



Evidence for CP -Violating Asymmetries in $B^0 \rightarrow \pi^+ \pi^-$ Decays and Constraints on the CKM Angle ϕ_2

K. Abe,⁷ K. Abe,⁴¹ N. Abe,⁴⁴ T. Abe,⁴² I. Adachi,⁷ H. Aihara,⁴³ K. Akai,⁷ M. Akatsu,²¹ M. Akemoto,⁷ Y. Asano,⁴⁷ T. Aushev,¹¹ A. M. Bakich,³⁹ Y. Ban,³² E. Banas,²⁶ A. Bay,¹⁷ I. Bedny,² P. K. Behera,⁴⁸ I. Bizjak,¹² A. Bondar,² A. Bozek,²⁶ M. Bračko,^{19, 12} J. Brodzicka,²⁶ T. E. Browder,⁶ B. C. K. Casey,⁶ P. Chang,²⁵ K.-F. Chen,²⁵ B. G. Cheon,³⁸ R. Chistov,¹¹ S.-K. Choi,⁵² Y. Choi,³⁸ Y. K. Choi,³⁸ M. Danilov,¹¹ J. Dragic,²⁰ A. Drutskoy,¹¹ S. Eidelman,² V. Eiges,¹¹ C. W. Everton,²⁰ J. Flanagan,⁷ C. Fukunaga,⁴⁵ K. Furukawa,⁷ N. Gabyshev,⁷ A. Garmash,^{2, 7} T. Gershon,⁷ B. Golob,^{18, 12} R. Guo,²³ C. Hagner,⁴⁹ K. Hara,³⁰ N. C. Hastings,⁷ K. Hasuko,³⁴ H. Hayashii,²² M. Hazumi,⁷ T. Higuchi,⁷ L. Hinz,¹⁷ T. Hojo,³⁰ T. Hokuue,²¹ Y. Hoshi,⁴¹ W.-S. Hou,²⁵ Y. B. Hsiung,²⁵ H.-C. Huang,²⁵ T. Igaki,²¹ Y. Igarashi,⁷ T. Iijima,²¹ H. Ikeda,⁷ K. Inami,²¹ A. Ishikawa,²¹ H. Ishino,⁴⁴ R. Itoh,⁷ H. Iwasaki,⁷ Y. Iwasaki,⁷ H. K. Jang,³⁷ J. S. Kang,¹⁴ P. Kapusta,²⁶ S. U. Kataoka,²² N. Katayama,⁷ G. Katano,⁷ H. Kawai,⁴³ N. Kawamura,¹ T. Kawasaki,²⁸ H. Kichimi,⁷ M. Kikuchi,⁷ E. Kikutani,⁷ D. W. Kim,³⁸ H. J. Kim,⁵¹ H. O. Kim,³⁸ Hyunwoo Kim,¹⁴ J. H. Kim,³⁸ S. K. Kim,³⁷ S. Kobayashi,³⁵ S. Korpar,^{19, 12} P. Križan,^{18, 12} P. Krokovny,² T. Kubo,⁷ R. Kulasiri,⁴ S. Kumar,³¹ A. Kuzmin,² Y.-J. Kwon,⁵¹ J. S. Lange,^{5, 34} G. Leder,¹⁰ S. H. Lee,³⁷ J. Li,³⁶ S.-W. Lin,²⁵ J. MacNaughton,¹⁰ F. Mandl,¹⁰ D. Marlow,³³ S. Matsumoto,³ T. Matsumoto,⁴⁵ S. Michizono,⁷ T. Mimashi,⁷ W. Mitaroff,¹⁰ K. Miyabayashi,²² H. Miyake,³⁰ H. Miyata,²⁸ T. Mori,³ A. Murakami,³⁵ Y. Nagasaka,⁸ T. Nakadaira,⁴³ T. T. Nakamura,⁷ E. Nakano,²⁹ M. Nakao,⁷ H. Nakayama,⁷ J. W. Nam,³⁸ K. Neichi,⁴¹ S. Nishida,¹⁵ O. Nitoh,⁴⁶ S. Noguchi,²² T. Nozaki,⁷ S. Ogawa,⁴⁰ Y. Ogawa,⁷ K. Ohmi,⁷ Y. Ohnishi,⁷ T. Ohshima,²¹ N. Ohuchi,⁷ T. Okabe,²¹ S. Okuno,¹³ S. L. Olsen,⁶ Y. Onuki,²⁸ W. Ostrowicz,²⁶ H. Ozaki,⁷ H. Palka,²⁶ C. W. Park,¹⁴ H. Park,¹⁶ K. S. Park,³⁸ L. S. Peak,³⁹ J.-P. Perroud,¹⁷ M. Peters,⁶ L. E. Piilonen,⁴⁹ M. Rozanska,²⁶ K. Rybicki,²⁶ H. Sagawa,⁷ S. Saitoh,⁷ Y. Sakai,⁷ T. R. Sarangi,⁴⁸ M. Satapathy,⁴⁸ A. Satpathy,^{7, 4} O. Schneider,¹⁷ S. Schrenk,⁴ J. Schümann,²⁵ C. Schwanda,^{7, 10} S. Semenov,¹¹ K. Senyo,²¹ M. E. Sevior,²⁰ H. Shibuya,⁴⁰ T. Shidara,⁷ B. Shwartz,² V. Sidorov,² J. B. Singh,³¹ S. Stanič,^{7, *} M. Starič,¹² R. Sugahara,⁷ A. Sugiyama,²¹ K. Sumisawa,⁷ T. Sumiyoshi,⁴⁵ K. Suzuki,⁷ S. Suzuki,⁵⁰ T. Takahashi,²⁹ F. Takasaki,⁷ K. Tamai,⁷ N. Tamura,²⁸ J. Tanaka,⁴³ M. Tanaka,⁷ M. Tawada,⁷ G. N. Taylor,²⁰ Y. Teramoto,²⁹ S. Tokuda,²¹ T. Tomura,⁴³ K. Trabelsi,⁶ T. Tsuboyama,⁷ T. Tsukamoto,⁷ S. Uehara,⁷ Y. Unno,⁵³ S. Uno,⁷ N. Uozaki,⁴³ S. E. Vahsen,³³ G. Varner,⁶ K. E. Varvell,³⁹ C. C. Wang,²⁵ C. H. Wang,²⁴ J. G. Wang,⁴⁹ M.-Z. Wang,²⁵ Y. Watanabe,⁴⁴ E. Won,¹⁴ B. D. Yabsley,⁴⁹ Y. Yamada,⁷ A. Yamaguchi,⁴² H. Yamamoto,⁴² Y. Yamashita,²⁷ Y. Yamashita,⁴³ M. Yamauchi,⁷ M. Yokoyama,⁴³ M. Yoshida,⁷ C. C. Zhang,⁹ Z. P. Zhang,³⁶ V. Zhilich,² and D. Žontar^{18, 12}

(The Belle Collaboration)

¹*Aomori University, Aomori*

²*Budker Institute of Nuclear Physics, Novosibirsk*

³*Chuo University, Tokyo*

⁴*University of Cincinnati, Cincinnati, Ohio 45221*

⁵*University of Frankfurt, Frankfurt*

⁶*University of Hawaii, Honolulu, Hawaii 96822*

⁷*High Energy Accelerator Research Organization (KEK), Tsukuba*

⁸*Hiroshima Institute of Technology, Hiroshima*

⁹*Institute of High Energy Physics, Chinese Academy of Sciences, Beijing*

¹⁰*Institute of High Energy Physics, Vienna*

¹¹*Institute for Theoretical and Experimental Physics, Moscow*

¹²*J. Stefan Institute, Ljubljana*

¹³*Kanagawa University, Yokohama*

¹⁴*Korea University, Seoul*

¹⁵*Kyoto University, Kyoto*

¹⁶*Kyungpook National University, Taegu*

¹⁷*Institut de Physique des Hautes Énergies, Université de Lausanne, Lausanne*

¹⁸*University of Ljubljana, Ljubljana*

¹⁹*University of Maribor, Maribor*

²⁰*University of Melbourne, Victoria*

²¹*Nagoya University, Nagoya*

²²*Nara Women's University, Nara*

²³*National Kaohsiung Normal University, Kaohsiung*

²⁴*National Lien-Ho Institute of Technology, Miao Li*

²⁵*National Taiwan University, Taipei*

²⁶*H. Niewodniczanski Institute of Nuclear Physics, Krakow*

²⁷*Nihon Dental College, Niigata*

²⁸*Niigata University, Niigata*

²⁹*Osaka City University, Osaka*

³⁰*Osaka University, Osaka*

³¹*Panjab University, Chandigarh*

³²*Peking University, Beijing*

³³*Princeton University, Princeton, New Jersey 08545*

³⁴*RIKEN BNL Research Center, Upton, New York 11973*

³⁵*Saga University, Saga*

³⁶*University of Science and Technology of China, Hefei*

³⁷*Seoul National University, Seoul*

³⁸*Sungkyunkwan University, Suwon*

³⁹*University of Sydney, Sydney NSW*

⁴⁰*Toho University, Funabashi*

⁴¹*Tohoku Gakuin University, Tagajo*

⁴²*Tohoku University, Sendai*

⁴³*University of Tokyo, Tokyo*

⁴⁴*Tokyo Institute of Technology, Tokyo*

⁴⁵*Tokyo Metropolitan University, Tokyo*

⁴⁶*Tokyo University of Agriculture and Technology, Tokyo*

⁴⁷*University of Tsukuba, Tsukuba*

⁴⁸*Utkal University, Bhubaneswer*

⁴⁹*Virginia Polytechnic Institute and State University, Blacksburg, Virginia 24061*

⁵⁰*Yokkaichi University, Yokkaichi*

⁵¹*Yonsei University, Seoul*

⁵²*Gyeongsang National University, Chinju*

⁵³*Chiba University, Chiba*

(Dated: January 29, 2020)

Abstract

We present an improved measurement of CP -violating asymmetries in $B^0 \rightarrow \pi^+ \pi^-$ decays based on a 78 fb^{-1} data sample collected at the $\Upsilon(4S)$ resonance with the Belle detector at the KEKB asymmetric-energy $e^+ e^-$ collider. We reconstruct one neutral B meson as a $B^0 \rightarrow \pi^+ \pi^-$ CP eigenstate and identify the flavor of the accompanying B meson from inclusive properties of its decay products. We apply an unbinned maximum likelihood fit to the distribution of the time intervals between the two B meson decay points. The fit yields the CP -violating asymmetry amplitudes $\mathcal{A}_{\pi\pi} = +0.77 \pm 0.27(\text{stat}) \pm 0.08(\text{syst})$ and $\mathcal{S}_{\pi\pi} = -1.23 \pm 0.41(\text{stat})^{+0.08}_{-0.07}(\text{syst})$, where the statistical uncertainties are determined from Monte Carlo pseudo-experiments. We obtain confidence intervals for CP -violating asymmetry parameters $\mathcal{A}_{\pi\pi}$ and $\mathcal{S}_{\pi\pi}$ based on a frequentist approach. We rule out the CP -conserving case, $\mathcal{A}_{\pi\pi} = \mathcal{S}_{\pi\pi} = 0$, at the 99.93% confidence level. We discuss how these results constrain the value of the CKM angle ϕ_2 .

PACS numbers: 11.30.Er, 12.15.Hh, 13.25.Hw

^{*}on leave from Nova Gorica Polytechnic, Nova Gorica

I. INTRODUCTION

In 1973, Kobayashi and Maskawa (KM) proposed a model where CP violation is accommodated as an irreducible complex phase in the weak-interaction quark mixing matrix [1]. Recent measurements of the CP -violating parameter $\sin 2\phi_1$ by the Belle [2, 3] and BaBar [4] collaborations established CP violation in the neutral B meson system that is consistent with the KM model. Measurements of other CP -violating parameters provide important tests of the KM model.

The KM model predicts CP -violating asymmetries in the time-dependent rates for B^0 and \bar{B}^0 decays to a common CP eigenstate, f_{CP} [5]. In the decay chain $\Upsilon(4S) \rightarrow B^0 \bar{B}^0 \rightarrow f_{CP} f_{tag}$, in which one of the B mesons decays at time t_{CP} to f_{CP} and the other decays at time t_{tag} to a final state f_{tag} that distinguishes between B^0 and \bar{B}^0 , the decay rate has a time dependence given by [6]

$$\mathcal{P}_{\pi\pi}^q(\Delta t) = \frac{e^{-|\Delta t|/\tau_{B^0}}}{4\tau_{B^0}} [1 + q \cdot \{\mathcal{S}_{\pi\pi} \sin(\Delta m_d \Delta t) + \mathcal{A}_{\pi\pi} \cos(\Delta m_d \Delta t)\}], \quad (1)$$

where τ_{B^0} is the B^0 lifetime, Δm_d is the mass difference between the two B^0 mass eigenstates, $\Delta t = t_{CP} - t_{tag}$, and the b -flavor charge $q = +1$ (-1) when the tagging B meson is a B^0 (\bar{B}^0). The CP -violating parameters $\mathcal{S}_{\pi\pi}$ and $\mathcal{A}_{\pi\pi}$ defined in Eq. (1) are expressed as

$$\mathcal{A}_{\pi\pi} = \frac{|\lambda|^2 - 1}{|\lambda|^2 + 1}, \quad \mathcal{S}_{\pi\pi} = \frac{2Im\lambda}{|\lambda|^2 + 1}, \quad (2)$$

where λ is a complex parameter that depends on both B^0 - \bar{B}^0 mixing and on the amplitudes for B^0 and \bar{B}^0 decay to $\pi^+\pi^-$. In the Standard Model, to a good approximation, $|\lambda|$ is equal to the absolute value of the ratio of the \bar{B}^0 to B^0 decay amplitudes. A measurement of time-dependent CP -violating asymmetries in the mode $B^0 \rightarrow \pi^+\pi^-$ [7] is sensitive to direct CP violation and the CKM angle ϕ_2 [8]. If the decay proceeded only via a $b \rightarrow u$ tree amplitude, we would have $\mathcal{S}_{\pi\pi} = \sin 2\phi_2$ and $\mathcal{A}_{\pi\pi} = 0$, or equivalently $|\lambda| = 1$. The situation is complicated by the possibility of significant contributions from gluonic $b \rightarrow d$ penguin amplitudes that have a different weak phase and additional strong phases [9]. As a result, $\mathcal{S}_{\pi\pi}$ may not be equal to $\sin 2\phi_2$ and direct CP violation, $\mathcal{A}_{\pi\pi} \neq 0$, may occur.

Belle's earlier published study [10] was based on a 41.8 fb^{-1} data sample containing $44.8 \times 10^6 B\bar{B}$ pairs produced at the $\Upsilon(4S)$ resonance. The result suggested large direct CP asymmetry and/or mixing-induced asymmetry in $B^0 \rightarrow \pi^+\pi^-$ decay while the corresponding result by the BaBar collaboration based on a similarly sized data sample did not [11]. In this paper, we report an updated measurement that is based on a 78 fb^{-1} data sample, containing $85 \times 10^6 B\bar{B}$ pairs. The most important change is that we determine the statistical significance and uncertainties in the CP parameters from the distributions of the results of fits to Monte Carlo (MC) pseudo-experiments, instead of from errors obtained by the likelihood fit to experimental data. In addition, we have made three significant improvements to the analysis: a new track reconstruction algorithm that provides better performance; a new proper-time interval resolution function that reduces systematic uncertainties; and the inclusion of additional signal candidates by optimizing the cuts for continuum background suppression.

In Sec. II we describe the KEKB collider and the Belle detector. The reconstruction of $B^0 \rightarrow \pi^+\pi^-$ decays is described in Sec. III. The flavor-tagging procedure and vertex

reconstruction are described in Secs. IV and V. After discussing the signal yield in Sec. VI and introducing the method to measure $\mathcal{A}_{\pi\pi}$ and $\mathcal{S}_{\pi\pi}$ from Δt distributions in Sec. VII, we present the results of the fit in Sec. VIII, and discuss constraints on ϕ_2 in Sec. IX. We summarize the results in Sec. X.

II. EXPERIMENTAL APPARATUS

The data reported here were collected with the Belle detector at the KEKB asymmetric-energy e^+e^- collider [12], which collides 8.0 GeV e^- and 3.5 GeV e^+ beams at a small (± 11 mrad) crossing angle. The $\Upsilon(4S)$ is produced with a Lorentz boost of $\beta\gamma = 0.425$ nearly along the electron beamline (z). Since the B^0 and \bar{B}^0 mesons are approximately at rest in the $\Upsilon(4S)$ center-of-mass system (cms), Δt can be determined from Δz , the displacement in z between the f_{CP} and f_{tag} decay vertices: $\Delta t \simeq (z_{CP} - z_{tag})/\beta\gamma c \equiv \Delta z/\beta\gamma c$.

The Belle detector is a large-solid-angle general purpose spectrometer that consists of a silicon vertex detector (SVD), a central drift chamber (CDC), an array of aerogel threshold Čerenkov counters (ACC), time-of-flight scintillation counters, and an electromagnetic calorimeter comprised of CsI(Tl) crystals located inside a superconducting solenoid coil that provides a 1.5 T magnetic field. An iron flux return located outside of the coil is instrumented to detect K_L^0 mesons and muons. For more details, see Ref. [13].

III. RECONSTRUCTION OF $B^0 \rightarrow \pi^+\pi^-$ DECAYS

The $B^0 \rightarrow \pi^+\pi^-$ event selection is described in detail elsewhere [14]. We use oppositely charged track pairs that are positively identified as pions according to the likelihood ratio for a particle to be a K^\pm meson, $\text{KID} = \mathcal{L}(K)/[\mathcal{L}(K) + \mathcal{L}(\pi)]$, which is based on the combined information from the ACC and the CDC dE/dx measurements. Here we use $\text{KID} < 0.4$ as the default requirement for the selection of pions. This requirement has a pion efficiency of 91% and a misidentification rate from kaons of 10% for the $B^0 \rightarrow \pi^+\pi^-$ tracks.

We also select $B^0 \rightarrow K^+\pi^-$ candidates, which have the same track topology as $B^0 \rightarrow \pi^+\pi^-$ candidates, by positively identifying one charged track as a kaon and the other as a pion. We use $\text{KID} > 0.6$ for the selection of kaons. This requirement has a kaon efficiency of 84% and a misidentification rate from pions of 5%.

Candidate B mesons are reconstructed using the energy difference $\Delta E \equiv E_B^{\text{cms}} - E_{\text{beam}}^{\text{cms}}$ and the beam-energy constrained mass $M_{\text{bc}} \equiv \sqrt{(E_{\text{beam}}^{\text{cms}})^2 - (p_B^{\text{cms}})^2}$, where $E_{\text{beam}}^{\text{cms}}$ is the cms beam energy, and E_B^{cms} and p_B^{cms} are the cms energy and momentum of the B candidate. The signal region is defined as $5.271 \text{ GeV}/c^2 < M_{\text{bc}} < 5.287 \text{ GeV}/c^2$ and $|\Delta E| < 0.057 \text{ GeV}$, corresponding to $\pm 3\sigma$ from the central values. In order to suppress background from the $e^+e^- \rightarrow q\bar{q}$ continuum ($q = u, d, s, c$), we form signal and background likelihood functions, \mathcal{L}_S and \mathcal{L}_{BG} , from two variables. One is a Fisher discriminant determined from six modified Fox-Wolfram moments [15]; the other is the cms B flight direction with respect to the z axis. We determine \mathcal{L}_S from a GEANT-based Monte Carlo (MC) simulation [16], and \mathcal{L}_{BG} from sideband data in the $5.20 \text{ GeV}/c^2 < M_{\text{bc}} < 5.26 \text{ GeV}/c^2$ and $-0.3 \text{ GeV} < \Delta E < 0.5 \text{ GeV}$ region. We reduce the continuum background by imposing requirements on the likelihood ratio $LR = \mathcal{L}_S/(\mathcal{L}_S + \mathcal{L}_{BG})$ for candidate events, as described below.

IV. FLAVOR TAGGING

Leptons, kaons, and charged pions that are not associated with the reconstructed $B^0 \rightarrow \pi^+ \pi^-$ decay are used to identify the flavor of the accompanying B meson. We apply the same method used for the Belle $\sin 2\phi_1$ measurement [3]. We use two parameters, q and r , to represent the tagging information. The first, q , is defined in Eq. (1). The parameter r is an event-by-event, MC-determined flavor-tagging dilution factor that ranges from $r = 0$ for no flavor discrimination to $r = 1$ for unambiguous flavor assignment. It is used only to sort data into six r intervals. The wrong tag fractions for the six r intervals, w_l ($l = 1, 6$), are determined from the data and are summarized in Table I.

TABLE I: The wrong tag fraction w_l for each r interval. The errors include both statistical and systematic uncertainties.

| l | r interval | w_l |
|-----|---------------|-------------------|
| 1 | 0.000 – 0.250 | 0.458 ± 0.007 |
| 2 | 0.250 – 0.500 | 0.336 ± 0.010 |
| 3 | 0.500 – 0.625 | 0.228 ± 0.011 |
| 4 | 0.625 – 0.750 | 0.160 ± 0.014 |
| 5 | 0.750 – 0.875 | 0.112 ± 0.015 |
| 6 | 0.875 – 1.000 | 0.020 ± 0.007 |

In the previous publication [10], we required $LR > 0.825$ for each flavor tagging interval r in order to suppress the continuum background. In this analysis, we optimize the expected sensitivity by including additional events with $LR < 0.825$ for each r interval. This results in twelve distinct regions ($m = 1, 12$) in the LR - r plane. The LR requirements vary for different regions as shown in Table II.

V. VERTEX RECONSTRUCTION

The vertex reconstruction algorithm is the same as that used for the $\sin 2\phi_1$ analysis [3]. The vertex positions for the f_{CP} decay ($\pi^+ \pi^-$) and f_{tag} decays are reconstructed using tracks with associated hits in the SVD. Each vertex position is also constrained by the interaction point profile, determined run-by-run, smeared in the r - ϕ plane to account for the B meson decay length. With these requirements, we are able to determine a vertex even with a single track; the fraction of single-track vertices is about 10% for z_{CP} and 22% for z_{tag} . The f_{tag} vertex is determined from all well-reconstructed tracks, excluding the $B^0 \rightarrow \pi^+ \pi^-$ tracks and tracks that form a K_S^0 candidate.

VI. SIGNAL YIELD

Figures 1(a) and (b) show the ΔE distributions for the $B^0 \rightarrow \pi^+ \pi^-$ candidates that are in the M_{bc} signal region with $LR > 0.825$ and with $LR \leq 0.825$, respectively, after flavor tagging and vertex reconstruction. In the M_{bc} and ΔE signal region, we find 275 candidates for $LR > 0.825$ and 485 candidates for $LR \leq 0.825$. The $B^0 \rightarrow \pi^+ \pi^-$ signal yield for $LR > 0.825$ is extracted by fitting the ΔE distribution with a Gaussian signal function plus contributions

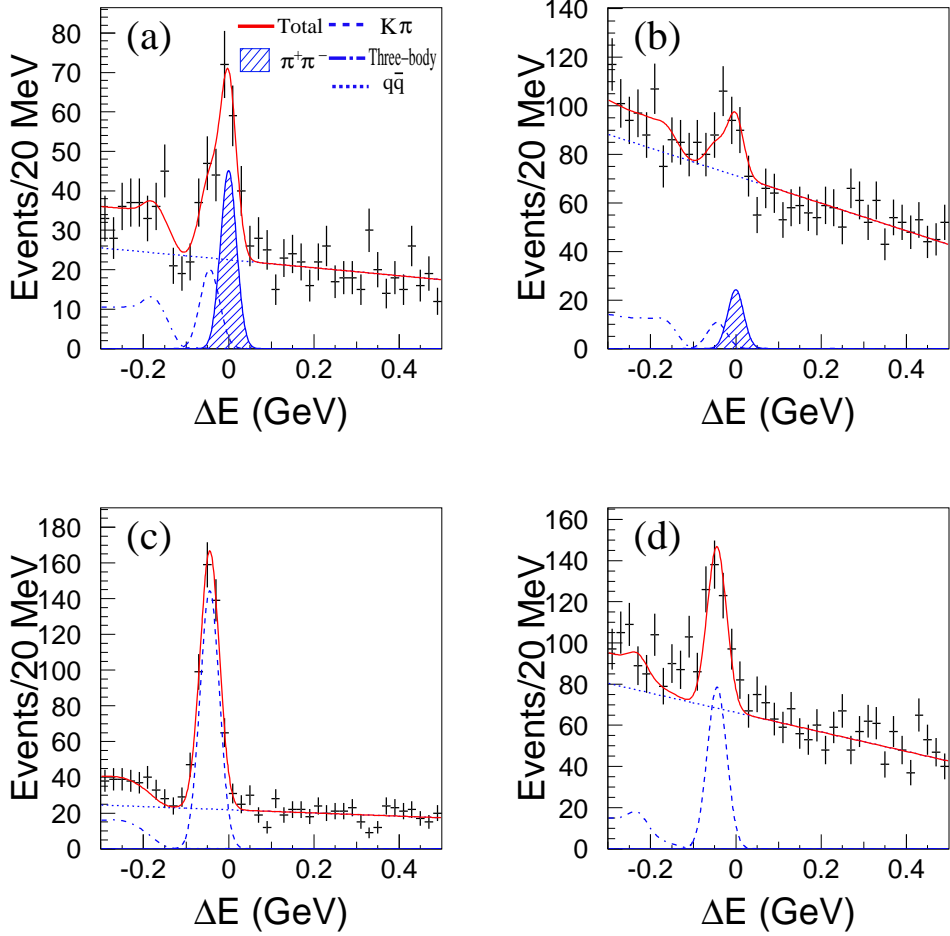


FIG. 1: ΔE distributions in the M_{bc} signal region for (a) $B^0 \rightarrow \pi^+\pi^-$ candidates with $LR > 0.825$, (b) $B^0 \rightarrow \pi^+\pi^-$ candidates with $LR \leq 0.825$, (c) $B^0 \rightarrow K^+\pi^-$ candidates with $LR > 0.825$, and (d) $B^0 \rightarrow K^+\pi^-$ candidates with $LR \leq 0.825$. The sum of the signal and background functions is shown as a solid curve. The solid curve with hatched area represents the $\pi^+\pi^-$ component, the dashed curve represents the $K^+\pi^-$ component, the dotted curve represents the continuum background, and the dot-dashed curve represents the charmless three-body B decay background component.

from misidentified $B^0 \rightarrow K^+\pi^-$ events, three-body B -decays, and continuum background. The fit yields 106^{+16}_{-15} $\pi^+\pi^-$ events, 41^{+10}_{-9} $K^+\pi^-$ events and 128^{+5}_{-6} continuum events in the signal region. The errors do not include systematic uncertainties unless otherwise stated. For the fit to the events with $LR \leq 0.825$, we fix the level of $K^+\pi^-$ background by scaling the $LR > 0.825$ number by a MC-determined factor and that of the continuum background from the sideband data. We obtain 57 ± 8 $\pi^+\pi^-$ events, 22^{+6}_{-5} $K^+\pi^-$ events and 406 ± 17 continuum events in the signal region for $LR \leq 0.825$. The contribution from three-body B -decays is negligibly small in the signal region. Figures 1(c) and (d) show the ΔE distributions for the selected $B^0 \rightarrow K^+\pi^-$ candidates.

VII. MAXIMUM LIKELIHOOD FIT

The proper-time interval resolution function $R_{\pi\pi}$ for $B^0 \rightarrow \pi^+\pi^-$ signal events is formed by convolving four components: the detector resolutions for z_{CP} and z_{tag} , the shift in the z_{tag} vertex position due to secondary tracks originating from charmed particle decays, and the smearing due to the kinematic approximation used to convert Δz to Δt . We use the same parameters as those used for the $\sin 2\phi_1$ measurement [3]. We determine resolution parameters from fitting the data for the neutral and charged B meson lifetimes. A small component of broad outliers in the Δz distribution, caused by mis-reconstruction, is represented by a Gaussian function. The width of the outlier component is determined to be 42^{+5}_{-4} ps; the fractions f_{ol} of the outlier components are $(2 \pm 1) \times 10^{-4}$ for events with both vertices reconstructed with more than one track, and $(2.7 \pm 0.2) \times 10^{-2}$ for events with one or two single-track vertices. We assume $R_{\pi\pi} = R_{K\pi}$ and denote them collectively as R_{sig} . The parameters of the continuum background resolution function $R_{q\bar{q}}$ are obtained from the sideband data.

The CP asymmetry parameters, $\mathcal{A}_{\pi\pi}$ and $\mathcal{S}_{\pi\pi}$, are obtained from an unbinned maximum likelihood fit to the observed proper-time distribution. For this purpose, we use probability density functions (PDFs) that are based on theoretical distributions that are diluted and smeared by the detector response. The PDF for $B^0 \rightarrow \pi^+\pi^-$ signal events ($\mathcal{P}_{\pi\pi}^q$) is given by Eq.(1), with q replaced by $q(1-2w_l)$ to account for the dilution due to wrong flavor tagging. The PDF for $B^0 \rightarrow K^+\pi^-$ background events is $\mathcal{P}_{K\pi}^q(\Delta t, w_l) = e^{-|\Delta t|/\tau_{B^0}}/(4\tau_{B^0})\{1 + q \cdot (1 - 2w_l) \cdot \mathcal{A}_{K\pi} \cdot \cos(\Delta m_d \Delta t)\}$, where we assume as a default that there is no CP asymmetry for the $B^0 \rightarrow K^+\pi^-$ mode. The effect of a possible non-zero value for $\mathcal{A}_{K\pi}$ is determined by varying $\mathcal{A}_{K\pi}$ by the error obtained from fits to the self-tagged $B^0 \rightarrow K^+\pi^-$ sample and is included in the systematic error. The PDF for continuum background events is $\mathcal{P}_{q\bar{q}}(\Delta t) = (1 + q \cdot \mathcal{A}_{bkg})/2\{f_\tau e^{-|\Delta t|/\tau_{bkg}}/(2\tau_{bkg}) + (1 - f_\tau)\delta(\Delta t)\}$, where f_τ is the fraction of the background with effective lifetime τ_{bkg} and δ is the Dirac delta function. For $B^0 \rightarrow \pi^+\pi^-$ events where both vertices have at least two tracks, we use $f_\tau = 0.014^{+0.006}_{-0.004}$ and $\tau_{bkg} = 2.37^{+0.44}_{-0.34}$ ps, which are determined from the events in the $q\bar{q}$ -background-dominated ΔE vs. M_{bc} sideband region. For events with a single-track vertex, we use $f_\tau = 0$. The effect of the uncertainty in \mathcal{A}_{bkg} , determined by varying \mathcal{A}_{bkg} by the error from the fit to the sideband data, is included in the systematic error.

We define the likelihood value for each (i -th) event as a function of $\mathcal{A}_{\pi\pi}$ and $\mathcal{S}_{\pi\pi}$:

$$P_i = (1 - f_{ol}) \int_{-\infty}^{+\infty} \{ (f_{\pi\pi}^m \mathcal{P}_{\pi\pi}^q(\Delta t', w_l; \mathcal{A}_{\pi\pi}, \mathcal{S}_{\pi\pi}) \\ + f_{K\pi}^m \mathcal{P}_{K\pi}^q(\Delta t', w_l)) \cdot R_{sig}(\Delta t_i - \Delta t') \\ + f_{q\bar{q}}^m \mathcal{P}_{q\bar{q}}(\Delta t') \cdot R_{q\bar{q}}(\Delta t_i - \Delta t') \} d\Delta t' + f_{ol} \mathcal{P}_{ol}(\Delta t_i). \quad (3)$$

Here the probability functions f_k^m ($k = \pi\pi$, $K\pi$ or $q\bar{q}$) are determined on an event-by-event basis as functions of ΔE and M_{bc} for each LR - r interval ($m = 1, 12$). For example, $f_{\pi\pi}^m(\Delta E, M_{bc})$ is $F_{\pi\pi}g_{\pi\pi}^m/(F_{q\bar{q}}^m g_{q\bar{q}}^m + F_{\pi\pi}g_{\pi\pi}^m + F_{K\pi}g_{K\pi}^m)$, where g_k^m is the average fraction of event-type k for the m -th LR - r interval ($g_{\pi\pi}^m + g_{K\pi}^m + g_{q\bar{q}}^m = 1$). We determine these parameters from the numbers of events in the sideband data and from fractions of $B^0 \rightarrow \pi^+\pi^-$ MC events. Table II lists the values of g_k^m for the 12 LR - r regions. We obtain $g_{K\pi}^m = 0.382 \times g_{\pi\pi}^m$ from the fit to the ΔE distribution for the $B^0 \rightarrow \pi^+\pi^-$ candidates with $LR > 0.85$. The distributions of ΔE and M_{bc} for the $B^0 \rightarrow \pi^+\pi^-$ signal shape function $F_{\pi\pi}(\Delta E, M_{bc})$ and $B^0 \rightarrow K^+\pi^-$ background shape function $F_{K\pi}(\Delta E, M_{bc})$ are fit with

Gaussian functions. $F_{q\bar{q}}^m(\Delta E, M_{bc})$ is the continuum background shape function, and the distributions of ΔE and M_{bc} are fit with m -dependent linear functions and the ARGUS background function [17], respectively. The small number of signal and background events that have large Δt are accommodated by the outlier PDF, \mathcal{P}_{ol} , with fractional area f_{ol} .

In the fit, $\mathcal{S}_{\pi\pi}$ and $\mathcal{A}_{\pi\pi}$ are free parameters determined by maximizing the likelihood function $\mathcal{L} = \prod_i P_i$, where the product is over all $B^0 \rightarrow \pi^+\pi^-$ candidates.

TABLE II: The fractions of expected $B^0 \rightarrow \pi^+\pi^-$ and continuum events for the 12 $LR\text{-}r$ regions.

| m | r interval | LR interval | $g_{\pi\pi}^m$ | $g_{q\bar{q}}^m$ |
|-----|---------------|---------------|-------------------|-------------------|
| 1 | 0.000 – 0.250 | 0.825 – 1.000 | 0.296 ± 0.077 | 0.591 ± 0.028 |
| 2 | 0.250 – 0.500 | 0.825 – 1.000 | 0.385 ± 0.094 | 0.468 ± 0.026 |
| 3 | 0.500 – 0.625 | 0.825 – 1.000 | 0.407 ± 0.134 | 0.438 ± 0.027 |
| 4 | 0.625 – 0.750 | 0.825 – 1.000 | 0.442 ± 0.110 | 0.389 ± 0.024 |
| 5 | 0.750 – 0.875 | 0.825 – 1.000 | 0.522 ± 0.081 | 0.279 ± 0.022 |
| 6 | 0.875 – 1.000 | 0.825 – 1.000 | 0.670 ± 0.129 | 0.074 ± 0.009 |
| 7 | 0.000 – 0.250 | 0.525 – 0.825 | 0.087 ± 0.034 | 0.880 ± 0.040 |
| 8 | 0.250 – 0.500 | 0.525 – 0.825 | 0.127 ± 0.049 | 0.824 ± 0.040 |
| 9 | 0.500 – 0.625 | 0.425 – 0.825 | 0.124 ± 0.036 | 0.829 ± 0.041 |
| 10 | 0.625 – 0.750 | 0.425 – 0.825 | 0.129 ± 0.050 | 0.822 ± 0.040 |
| 11 | 0.750 – 0.875 | 0.425 – 0.825 | 0.170 ± 0.060 | 0.765 ± 0.040 |
| 12 | 0.875 – 1.000 | 0.325 – 0.825 | 0.390 ± 0.098 | 0.461 ± 0.032 |

We check the validity of our fitting procedure with a large ensemble of MC pseudo-experiments wherein events are generated with nominal PDFs and the observed number of events. The parameters in the PDFs are taken from data. For various input values of $\mathcal{S}_{\pi\pi}$ and $\mathcal{A}_{\pi\pi}$, we confirm that there is no bias in the fit. The MC pseudo-experiments are described in detail in Appendix A.

VIII. FIT RESULTS

The unbinned maximum likelihood fit to the 760 $B^0 \rightarrow \pi^+\pi^-$ candidates (391 B^0 - and 369 \bar{B}^0 -tags), containing 163^{+24}_{-23} $\pi^+\pi^-$ signal events, yields $\mathcal{A}_{\pi\pi} = +0.77$ and $\mathcal{S}_{\pi\pi} = -1.23$. In Figs. 2(a) and (b), we show the raw, unweighted Δt distributions for the 148 B^0 - and 127 \bar{B}^0 -tagged events with $LR > 0.825$. The fit curves use $\mathcal{A}_{\pi\pi}$ and $\mathcal{S}_{\pi\pi}$ values that are obtained from all of the $LR\text{-}r$ regions. The background-subtracted Δt distributions are shown in Fig. 2(c). Figure 2(d) shows the background-subtracted CP asymmetry between the B^0 - and \bar{B}^0 -tagged events as a function of Δt . The result of the fit is superimposed and is shown by the solid curve.

We test the goodness-of-fit from a χ^2 comparison of the results of the unbinned fit and the Δt projections for $B^0 \rightarrow \pi^+\pi^-$ candidates [18]. We obtain $\chi^2 = 10.9/12$ DOF (13.3/12 DOF) for the Δt distribution of the B^0 (\bar{B}^0) tags.

As shown in Table III, an ensemble of MC pseudo-experiments indicates a 16.6% probability to measure CP violation at or above the one we observe when the input values are $\mathcal{A}_{\pi\pi} = +0.57$ and $\mathcal{S}_{\pi\pi} = -0.82$, which correspond to the values at the point of maximum

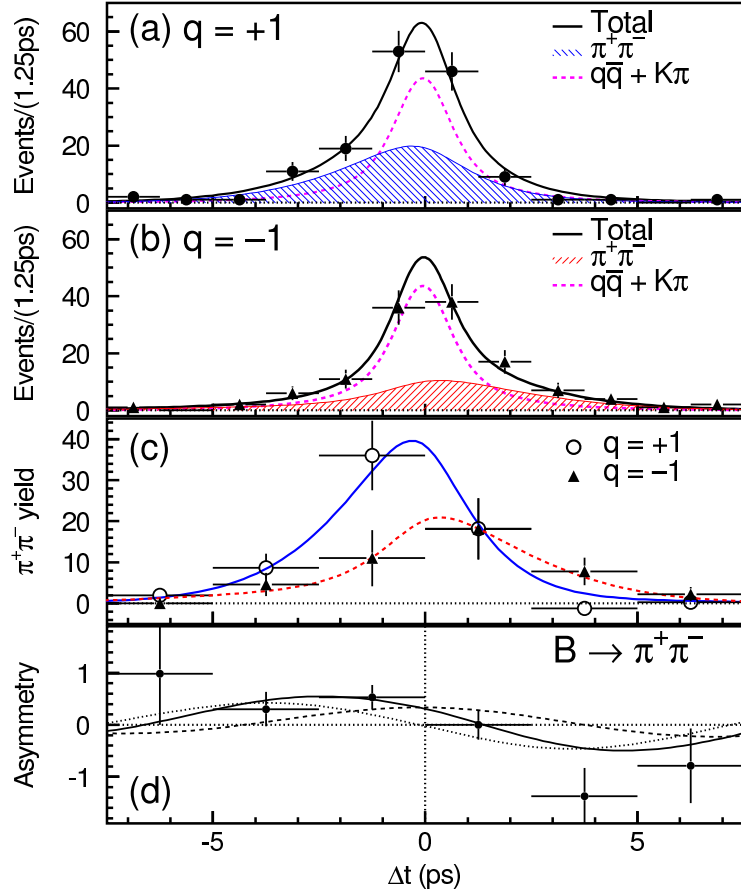


FIG. 2: The raw, unweighted Δt distributions for the 275 $B^0 \rightarrow \pi^+\pi^-$ candidates with $LR > 0.825$ in the signal region: (a) 148 candidates with $q = +1$, i.e. the tag side is identified as B^0 ; (b) 127 candidates with $q = -1$; (c) $B^0 \rightarrow \pi^+\pi^-$ yields after background subtraction. The errors are statistical only and do not include the error on the background subtraction; (d) the CP asymmetry for $B^0 \rightarrow \pi^+\pi^-$ after background subtraction. In Figs. (a) through (c), the curves show the results of the unbinned maximum likelihood fit to the Δt distributions of the 760 $B^0 \rightarrow \pi^+\pi^-$ candidates. In Fig. (d), the solid curve shows the resultant CP asymmetry, while the dashed (dotted) curve is the contribution from the cosine (sine) term.

likelihood in the physically allowed region ($\mathcal{S}_{\pi\pi}^2 + \mathcal{A}_{\pi\pi}^2 \leq 1$); in this measurement it is located at the physical boundary ($\mathcal{A}_{\pi\pi}^2 + \mathcal{S}_{\pi\pi}^2 = 1$). This set of MC pseudo-experiments also indicates that for an input value on the physical boundary, the probability of obtaining a result outside the physically allowed region is large (60.1%).

A. Statistical errors

As described below in Section VIIID, we obtain confidence intervals for $\mathcal{A}_{\pi\pi}$ and $\mathcal{S}_{\pi\pi}$ with a frequentist approach where we use MC pseudo-experiments to determine acceptance regions, and we quote the rms values of the MC $\mathcal{A}_{\pi\pi}$ and $\mathcal{S}_{\pi\pi}$ distributions as the errors of our measurement. We obtain $\mathcal{A}_{\pi\pi} = +0.77 \pm 0.27(\text{stat})$ and $\mathcal{S}_{\pi\pi} = -1.23 \pm 0.41(\text{stat})$.

TABLE III: The fractions of MC pseudo-experiments outside the physical boundary and above the CP violation we observe for various input values. $\rho_{\pi\pi} = \sqrt{\mathcal{A}_{\pi\pi}^2 + \mathcal{S}_{\pi\pi}^2}$. The selected points are on the line segment between $(\mathcal{A}_{\pi\pi}, \mathcal{S}_{\pi\pi}) = (0,0)$ and $(+0.57, -0.82)$.

| Input $\rho_{\pi\pi}$ | The fractions outside the physical boundary (%) | The fractions above the CP violation we observe (%) |
|-----------------------|---|---|
| 0.00 | 1.8 | 0.07 |
| 0.20 | 3.3 | 0.17 |
| 0.40 | 7.3 | 0.62 |
| 0.60 | 16.4 | 1.7 |
| 0.80 | 34.4 | 6.0 |
| 1.00 | 60.1 | 16.6 |

Here we choose values at the point of maximum likelihood in the physically allowed region, $(\mathcal{A}_{\pi\pi}, \mathcal{S}_{\pi\pi}) = (+0.57, -0.82)$, for the input to the MC pseudo-experiments used to obtain the statistical errors. The rms values determined with input values of $(\mathcal{A}_{\pi\pi}, \mathcal{S}_{\pi\pi}) = (0, 0)$ are slightly different; for these input values we obtain ± 0.28 and ± 0.39 for the $\mathcal{A}_{\pi\pi}$ and $\mathcal{S}_{\pi\pi}$ errors, respectively.

In the literature, the statistical error is usually determined from the parameter dependence of the log-likelihood ratio $-2\ln(\mathcal{L}/\mathcal{L}_{\max})$ that is obtained from the fit. Here we call this estimator the MINOS error, which corresponds to the deviation from the best fit parameter when $-2\ln(\mathcal{L}/\mathcal{L}_{\max})$ is changed by one. The MINOS error is a convenient approximation for defining a 68.3% (1σ) confidence interval; however, care is needed when defining intervals at higher confidence levels. Figure 3 shows the log-likelihood ratio curves from our data, where deviations from parabolic behavior are evident; for example, 3σ from the MINOS error for $\mathcal{S}_{\pi\pi}$ is considerably smaller than a three-standard-deviation error defined by the deviation from the best fit parameter when $-2\ln(\mathcal{L}/\mathcal{L}_{\max})$ is changed by 9. The MINOS errors obtained from the curves are also smaller than the expectations from the MC pseudo-experiments, as shown in Fig. 4; the probability of obtaining a MINOS error smaller than that in our measurement is 1.2% (12.0%) for $\mathcal{S}_{\pi\pi}$ ($\mathcal{A}_{\pi\pi}$) [19]. These characteristics are reproduced in a fraction of the MC pseudo-experiments that have $\mathcal{A}_{\pi\pi}$ and $\mathcal{S}_{\pi\pi}$ input values that are close to the physical boundary. We therefore conclude that the errors derived from the MC pseudo-experiments, rather than the MINOS errors, are more appropriate as the standard errors for this measurement. We describe an investigation of the source of the small MINOS errors in Appendix B.

B. Systematic errors

The sources of the systematic error are listed in Table IV. We add each contribution in quadrature for the total systematic errors. We obtain

$$\begin{aligned}\mathcal{A}_{\pi\pi} &= +0.77 \pm 0.27(\text{stat}) \pm 0.08(\text{syst}), \\ \mathcal{S}_{\pi\pi} &= -1.23 \pm 0.41(\text{stat}) \pm 0.08(\text{syst}).\end{aligned}$$

The systematic error on $\mathcal{A}_{\pi\pi}$ is primarily due to uncertainties in the background fractions and the vertexing. For $\mathcal{S}_{\pi\pi}$, the background fractions and a possible fit bias near the physical

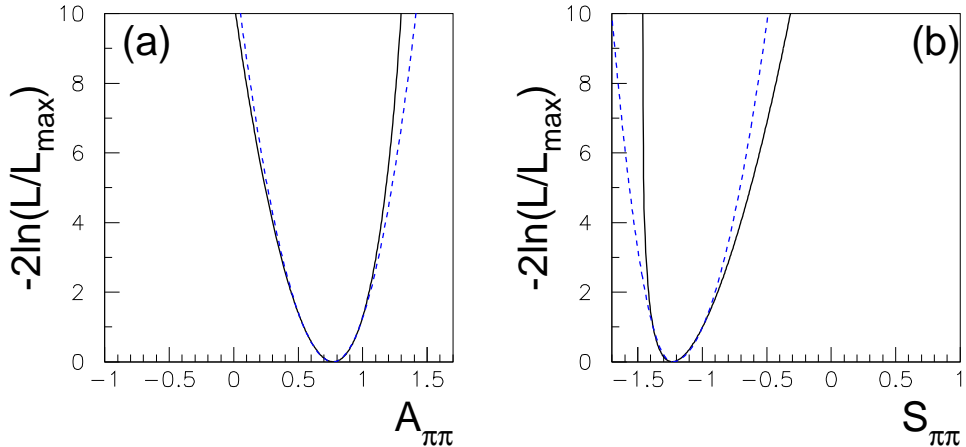


FIG. 3: (a) The value of $-2\ln(\mathcal{L}/\mathcal{L}_{\max})$ vs. $\mathcal{A}_{\pi\pi}$ and (b) the value of $-2\ln(\mathcal{L}/\mathcal{L}_{\max})$ vs. $\mathcal{S}_{\pi\pi}$. The dotted curves represent parabolic functions which pass the point at 1σ .

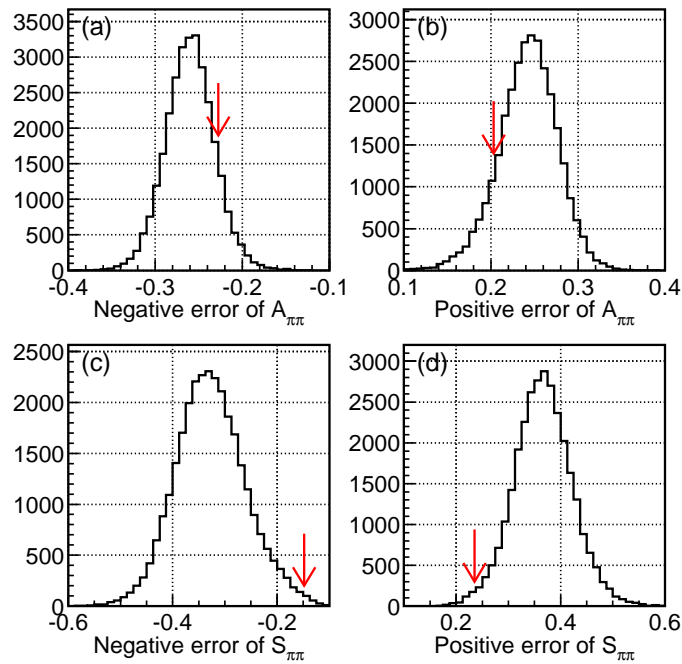


FIG. 4: The result of MC pseudo-experiments with input values of $\mathcal{A}_{\pi\pi} = +0.57$ and $\mathcal{S}_{\pi\pi} = -0.82$: the distributions of (a) the negative and (b) positive MINOS errors of $\mathcal{A}_{\pi\pi}$, and (c) the negative and (d) positive MINOS errors of $\mathcal{S}_{\pi\pi}$. The arrows indicate the MINOS errors obtained from the fit to data.

boundary are the two leading components. Below we explain each item in order.

TABLE IV: Systematic errors for $\mathcal{A}_{\pi\pi}$ and $\mathcal{S}_{\pi\pi}$.

| Source | $\mathcal{A}_{\pi\pi}$ | | $\mathcal{S}_{\pi\pi}$ | |
|--|------------------------|--------|------------------------|--------|
| | +error | -error | +error | -error |
| Background fractions | +0.058 | -0.048 | +0.044 | -0.055 |
| Vertexing | +0.044 | -0.054 | +0.037 | -0.012 |
| Fit bias | +0.016 | -0.021 | +0.052 | -0.020 |
| Wrong tag fraction | +0.026 | -0.021 | +0.015 | -0.016 |
| Physics (τ_{B^0} , Δm_d , $\mathcal{A}_{K\pi}$) | +0.021 | -0.014 | +0.022 | -0.022 |
| Resolution function | +0.019 | -0.020 | +0.010 | -0.013 |
| Background shape | +0.003 | -0.015 | +0.007 | -0.002 |
| Total | +0.084 | -0.083 | +0.083 | -0.067 |

1. Background fractions

We estimate the systematic errors that arise from uncertainties in the parameters used for the event-by-event background fractions $f_{K\pi}^m$ and $f_{q\bar{q}}^m$ as well as the signal fraction $f_{\pi\pi}^m$. Parameters that are determined from data are varied by their errors and fits are repeated; we add the contribution from each variation in quadrature.

As explained in Sec. VII, we rely on a MC $B^0 \rightarrow \pi^+\pi^-$ sample to determine g_k^m , the background fraction in each $LR\text{-}r$ region m . We measure the regional event fractions in $B^0 \rightarrow D^{(*)}\pi$ control samples, and compare the results with those in the MC $B^0 \rightarrow \pi^+\pi^-$ sample. Each g_k^m value is then modified by an amount determined from the difference between data and MC, and from the statistical error in the control samples. We repeat the fit to obtain $\mathcal{A}_{\pi\pi}$ and $\mathcal{S}_{\pi\pi}$, and add each difference from the nominal value in quadrature.

The $K\pi$ background yield is obtained from the fit to the ΔE distribution. We estimate the systematic error associated with this method from an independent yield measurement based on a $K\pi$ enriched-sample and the K/π separation performance, which will be described in Sec. VIII C.

The PDF for continuum background used in the fit assumes no asymmetry ($\mathcal{A}_{\text{bkg}} = 0$) between the number of events with $q = +1$ and with $q = -1$. We estimate the systematic error due to this assumption by varying \mathcal{A}_{bkg} by ± 0.02 , based on the measurement $\mathcal{A}_{\text{bkg}} = 0.013 \pm 0.006$ from the sideband data.

2. Vertexing

We search for possible biases that may arise from the track and vertex selection by repeating the analysis with modified selection criteria. We include the observed changes in the systematic error. We also repeat the analysis by introducing charge-dependent shifts in the z direction artificially, and include the resulting change in the systematic error. Here the amount of the shift is determined from studies with cosmic rays and with the two-photon process $e^+e^- \rightarrow \pi^+\pi^-\pi^+\pi^-$. The systematic error associated with the IP profile is estimated by varying the IP smearing that is used to account for the B flight length.

3. Fit bias and other sources

We use large-statistics MC pseudo-experiments to determine the systematic error due to possible fit biases for the input $\mathcal{A}_{\pi\pi}$ and $\mathcal{S}_{\pi\pi}$ values near the physical boundary. We also perform a fit to MC $B^0 \rightarrow \pi^+\pi^-$ events that are generated by using a GEANT-based simulation. We obtain results that are consistent with input values within the statistical errors, which are conservatively included in the systematic error.

Systematic errors due to uncertainties in the wrong tag fractions are estimated by varying each wrong tag fraction in each r region, and repeating the fit procedure. We also repeat the fit using wrong tag fractions obtained for B^0 - and \bar{B}^0 -tagged control samples separately. We add each contribution in quadrature.

We estimate the systematic errors associated with parameters in the resolution functions, in the background PDF, and the physics parameters (τ_{B^0} , Δm_d , and $\mathcal{A}_{K\pi}$) by repeating the fit varying these parameters by their errors.

C. Crosschecks

We perform a number of crosschecks. We measure the B meson lifetime using the same vertex reconstruction method. The results of the application of the same analysis to various subsamples are also examined. In addition, we check for biases in the analysis using samples of non- CP eigenstates, $B^0 \rightarrow K^+\pi^-$ decays, and sideband data.

We perform a B^0 lifetime measurement with the $B^0 \rightarrow \pi^+\pi^-$ candidate events that uses the same background fractions, vertex reconstruction methods, and resolution functions that are used for the CP fit. Figure 5(a) shows the fit result. The fit to the events in the $\pi^+\pi^-$ sideband is also shown in Fig. 5(c); the fit curve is used for the PDF of the continuum background. The result, $\tau_{B^0} = 1.42^{+0.14}_{-0.12}$ ps, is consistent with the world-average value [21].

We repeat the fits for $\mathcal{A}_{\pi\pi}$ and $\mathcal{S}_{\pi\pi}$ with $\pi^+\pi^-$ candidate samples selected with more stringent selection criteria. The $K^+\pi^-$ background level is reduced by tightening the accepted ΔE range or by applying more restrictive KID requirements; the continuum background is reduced by tighter requirements on LR and r . The effect of the Δt tail is checked by tightening the Δt range. We do not observe any systematic variation in the fit results when the ΔE , KID, LR , r , and Δt requirements are changed, as shown in Table V. To account for a possible ΔE tail, we repeat the fit with an additional Gaussian function in the ΔE shape of the $\pi^+\pi^-$ signal and the $K^+\pi^-$ background. The fit yields $\mathcal{A}_{\pi\pi} = +0.75$ and $\mathcal{S}_{\pi\pi} = -1.21$, consistent with our main results. In addition, we divide the data into the 42 fb^{-1} sample used for our previous measurement and the recently added sample of 36 fb^{-1} . The result of the new analysis on the first 42 fb^{-1} sample is consistent with the published result [10], and with that for the more recent 36 fb^{-1} sample.

A comparison of the event yields and Δt distributions for B^0 - and \bar{B}^0 -tagged events in the sideband region reveals no significant asymmetry as shown in Fig. 6(a). We also use samples of non- CP eigenstate $B^0 \rightarrow D^-\pi^+$, $D^{*-}\pi^+$ and $D^{*-}\rho^+$ decays, selected with the same event-shape criteria, to check for biases in the analysis. The combined fit to this control sample of 15321 events yields $\mathcal{A} = -0.015 \pm 0.022$ and $\mathcal{S} = 0.045 \pm 0.033$. The Δt distribution for this sample is shown in Fig. 6(b). As expected, neither mixing-induced nor direct CP -violating asymmetry is observed.

We select $B^0 \rightarrow K^+\pi^-$ candidates by positively identifying the charged kaons. A fit to the 1371 candidates (610 signal events) yields $\mathcal{A}_{K\pi} = -0.03 \pm 0.11$, in agreement with the

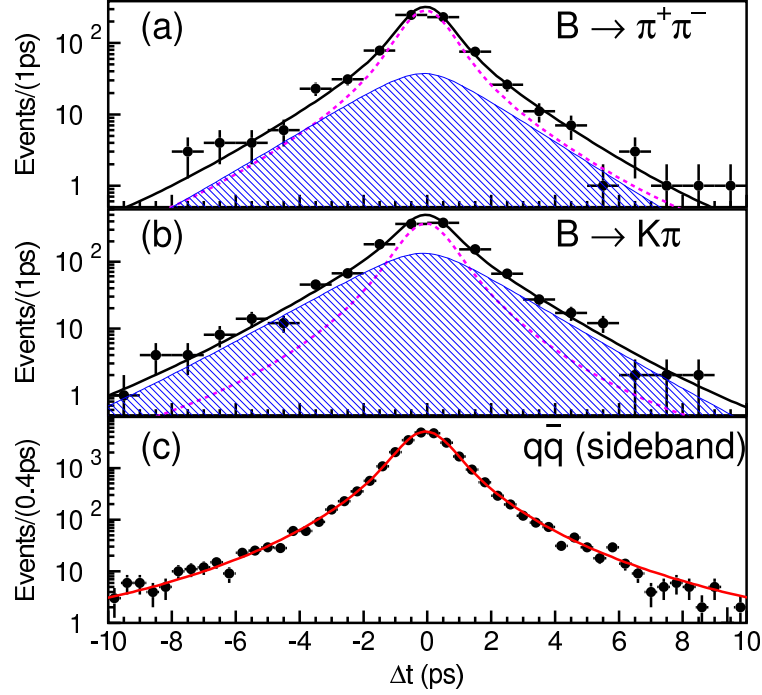


FIG. 5: Results of the lifetime fits for (a) $\pi^+\pi^-$ candidates and (b) $K^+\pi^-$ candidates. The solid curves are the results of the fits, the shaded areas are the signal and the dashed curves are background contributions. (c) The fit to events in the $\pi^+\pi^-$ sideband.

TABLE V: Selection-requirement dependence of $\mathcal{A}_{\pi\pi}$ and $\mathcal{S}_{\pi\pi}$ (MINOS errors only).

| Cut value | $\mathcal{A}_{\pi\pi}$ | $\mathcal{S}_{\pi\pi}$ |
|------------------------------------|------------------------|-------------------------|
| default (KID < 0.4) | $0.77^{+0.20}_{-0.23}$ | $-1.23^{+0.24}_{-0.15}$ |
| $ \Delta E < 2\sigma$ | $0.81^{+0.20}_{-0.22}$ | $-1.21^{+0.25}_{-0.16}$ |
| $ \Delta E < 1\sigma$ | $0.82^{+0.21}_{-0.25}$ | $-1.18^{+0.29}_{-0.19}$ |
| KID < 0.20 | $0.74^{+0.20}_{-0.23}$ | $-1.11^{+0.26}_{-0.17}$ |
| KID < 0.15 | $0.59^{+0.22}_{-0.24}$ | $-1.14^{+0.23}_{-0.14}$ |
| $LR > 0.825$ | $0.84^{+0.22}_{-0.25}$ | $-1.19^{+0.27}_{-0.18}$ |
| $LR > 0.925$ | $0.69^{+0.26}_{-0.30}$ | $-1.24^{+0.30}_{-0.19}$ |
| $ qr > 0.75$ | $1.02^{+0.19}_{-0.25}$ | $-1.24^{+0.19}_{-0.25}$ |
| $ qr > 0.875$ | $0.91^{+0.24}_{-0.31}$ | $-1.18^{+0.24}_{-0.31}$ |
| $ \Delta t < 15$ ps | $0.77^{+0.20}_{-0.23}$ | $-1.25^{+0.24}_{-0.15}$ |
| $ \Delta t < 5$ ps | $0.76^{+0.20}_{-0.22}$ | $-1.27^{+0.26}_{-0.17}$ |
| Sample I (42 fb^{-1}) | $1.00^{+0.19}_{-0.25}$ | $-1.14^{+0.30}_{-0.21}$ |
| Sample II (36 fb^{-1}) | $0.37^{+0.32}_{-0.33}$ | $-1.99^{+0.70}_{-0.65}$ |

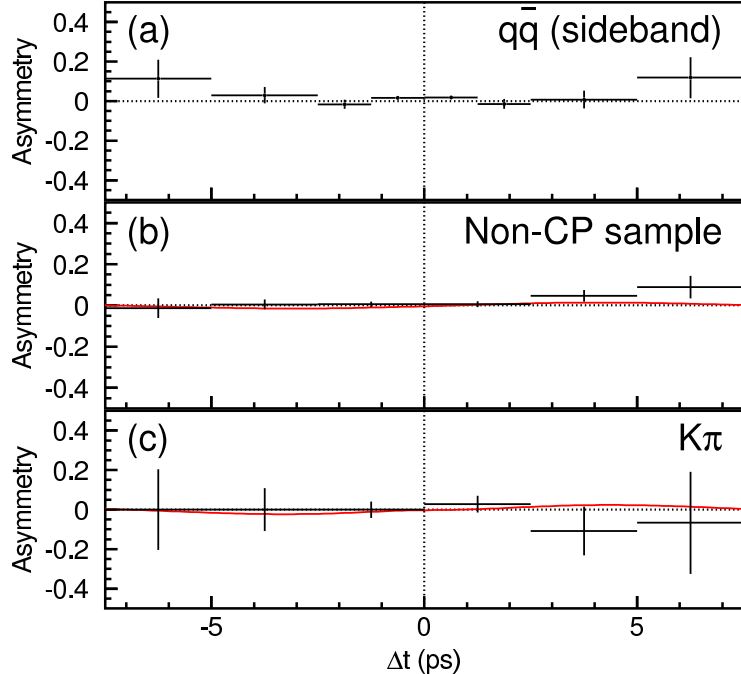


FIG. 6: The distributions of the raw Δt asymmetries for (a) $B^0 \rightarrow \pi^+ \pi^-$ sideband events, (b) the $B^0 \rightarrow D^- \pi^+$, $D^{*-} \pi^+$ and $D^{*-} \rho^+$ candidates combined and (c) $B^0 \rightarrow K^+ \pi^-$ candidates. Fit curves are also shown.

counting analysis mentioned above [20], and $\mathcal{S}_{K\pi} = 0.08 \pm 0.16$, which is consistent with zero as shown in Fig. 6(c). The MINOS errors for $\mathcal{A}_{K\pi}$ and $\mathcal{S}_{K\pi}$ are consistent with those from MC pseudo-experiment models of the $B^0 \rightarrow K^+ \pi^-$ measurement as shown in Fig. 7. With the $K^+ \pi^-$ event sample, we use the vertex reconstruction method and wrong-tag fractions described in Secs. IV and V and determine $\tau_{B^0} = 1.46 \pm 0.08$ ps [Fig. 5(b)] and $\Delta m_d = 0.55^{+0.05}_{-0.07}$ ps $^{-1}$, which are in agreement with the world average values [21].

The selected $K^+ \pi^-$ sample and the kaon mis-identification probability measured from a sample of inclusive $D^{*+} \rightarrow D^0(\rightarrow K^- \pi^+) \pi^+$ and $\phi \rightarrow K^+ K^-$ decays are used to make independent estimates of the $K^+ \pi^-$ background fractions in the $\pi^+ \pi^-$ sample. The results are 32 ± 2 $K^+ \pi^-$ events in the signal region with $LR > 0.825$ and 15 ± 2 $K^+ \pi^-$ events with $LR \leq 0.825$; these values are consistent with the results of the fit used to determine $\mathcal{S}_{\pi\pi}$ and $\mathcal{A}_{\pi\pi}$. The changes in $\mathcal{A}_{\pi\pi}^{(+0.005)}_{(-0.0)}$ and $\mathcal{S}_{\pi\pi}^{(+0.0)}_{(-0.03)}$ when these $K^+ \pi^-$ background fractions are used are included in the systematic error associated with the background fraction.

We check the measurement of $\mathcal{A}_{\pi\pi}$ using time-independent fits to the ΔE distributions for the B^0 and \bar{B}^0 tags. We determine the yields from fits to the ΔE distributions for each of the 12 LR - r bins for the B^0 and \bar{B}^0 tags separately (24 fits in total). We obtain $\mathcal{A}_{\pi\pi} = 0.56^{+0.26}_{-0.27}$, which is consistent with the time-dependent CP fit result.

As discussed above, the nominal fit result is outside of the physical region. We also consider fits that constrain the results to be in the physical region defined by $\mathcal{A}_{\pi\pi}^2 + \mathcal{S}_{\pi\pi}^2 \leq 1$. The disadvantage of the constrained fitting method is that when the fit result is close to the physical boundary, the errors returned from the fit are not Gaussian and are difficult to interpret. A constrained fit finds $\mathcal{A}_{\pi\pi} = +0.57$ and $\mathcal{S}_{\pi\pi} = -0.82$, on the boundary of the physical region; χ^2 values that are defined in Sec. VIII for the Δt projections are $\chi^2 =$

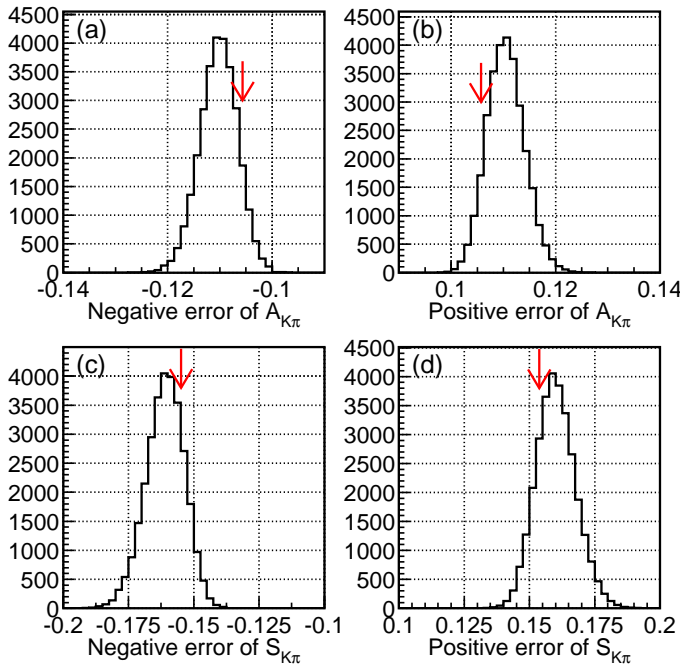


FIG. 7: The result of MC pseudo-experiments for $B^0 \rightarrow K^+\pi^-$ with input values of $\mathcal{A}_{K\pi} = -0.03$ and $\mathcal{S}_{K\pi} = 0.08$: the distributions of (a) the negative and (b) positive MINOS errors of $\mathcal{A}_{K\pi}$, and (c) the negative and (d) positive MINOS errors of $\mathcal{S}_{K\pi}$. The arrows indicate the MINOS errors obtained from the fit to data.

12.4/12 DOF (13.6/12 DOF) for the B^0 (\overline{B}^0) tag.

D. Significance

We use the Feldman-Cousins frequentist approach [22] to determine the statistical significance of our measurement. In order to form confidence intervals, we use the $\mathcal{A}_{\pi\pi}$ and $\mathcal{S}_{\pi\pi}$ distributions of the results of fits to MC pseudo-experiments for various input values of $\mathcal{A}_{\pi\pi}$ and $\mathcal{S}_{\pi\pi}$. The distributions incorporate possible biases at the boundary of the physical region as well as a correlation between $\mathcal{A}_{\pi\pi}$ and $\mathcal{S}_{\pi\pi}$; these effects are taken into account by this method. The distributions are also smeared with Gaussian functions that account for systematic errors. The details of the method used to obtain the confidence intervals are described in Appendix A. Figure 8 shows the resulting two-dimensional confidence regions in the $\mathcal{A}_{\pi\pi}$ vs. $\mathcal{S}_{\pi\pi}$ plane. The case that CP symmetry is conserved, $\mathcal{A}_{\pi\pi} = \mathcal{S}_{\pi\pi} = 0$, is ruled out at the 99.93% confidence level (C.L.), equivalent to 3.4σ significance for Gaussian errors. The minimum confidence level for $\mathcal{A}_{\pi\pi} = 0$, the case of no direct CP violation, occurs at $(\mathcal{S}_{\pi\pi}, \mathcal{A}_{\pi\pi}) = (-1.0, 0.0)$ and is 97.3%, which corresponds to 2.2σ significance.

If the source of CP violation is only due to $B - \overline{B}$ mixing or $\Delta B = 2$ transitions as in so-called superweak scenarios [23, 24], then $(\mathcal{S}_{\pi\pi}, \mathcal{A}_{\pi\pi}) = (-\sin 2\phi_1, 0)$. The C.L. at this point is 98.1%, equivalent to 2.3σ significance.

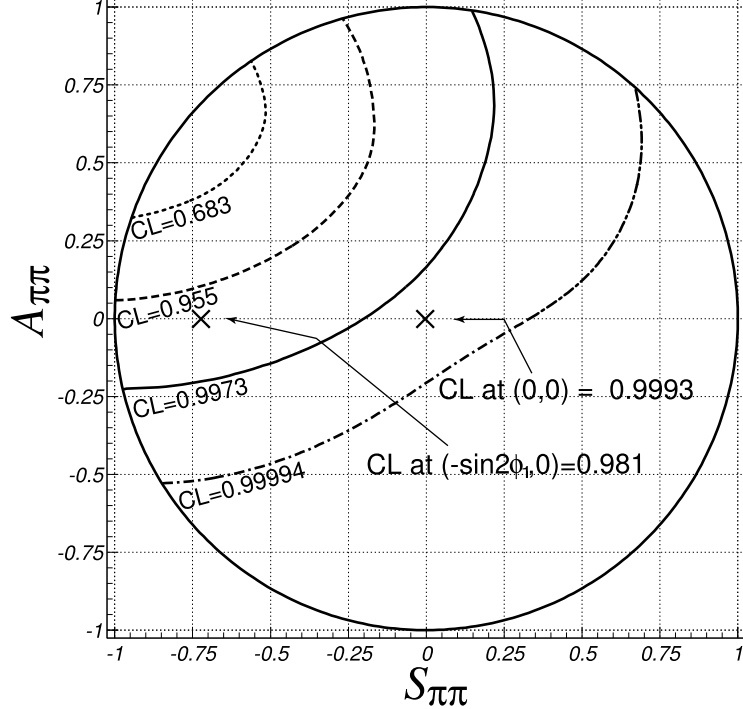


FIG. 8: Confidence regions for $\mathcal{A}_{\pi\pi}$ and $\mathcal{S}_{\pi\pi}$.

IX. DISCUSSION

Using the standard definitions of weak phases ϕ_1 , ϕ_2 , and ϕ_3 , the decay amplitudes for B^0 and \bar{B}^0 to $\pi^+\pi^-$ are

$$\begin{aligned} A(B^0 \rightarrow \pi^+\pi^-) &= -(|T|e^{i\delta_T}e^{i\phi_3} + |P|e^{i\delta_P}), \\ A(\bar{B}^0 \rightarrow \pi^+\pi^-) &= -(|T|e^{i\delta_T}e^{-i\phi_3} + |P|e^{i\delta_P}), \end{aligned} \quad (4)$$

where T and P are the amplitudes for the tree and penguin graphs and δ_T and δ_P are their strong phases. Here we adopt the notation of Ref. [25] and use the convention in which the top-quark contributions are integrated out in the short-distance effective Hamiltonian. In addition, the unitarity relation $V_{ub}^*V_{ud} + V_{cb}^*V_{cd} = -V_{tb}^*V_{td}$ is applied. Using the above expressions and $\phi_2 = \pi - \phi_1 - \phi_3$, we determine

$$\lambda_{\pi\pi} \equiv e^{2i\phi_2} \frac{1 + |P/T|e^{i(\delta+\phi_3)}}{1 + |P/T|e^{i(\delta-\phi_3)}}. \quad (5)$$

Explicit expressions for $\mathcal{S}_{\pi\pi}$ and $\mathcal{A}_{\pi\pi}$ are

$$\begin{aligned} \mathcal{S}_{\pi\pi} &= [\sin 2\phi_2 + 2|P/T|\sin(\phi_1 - \phi_2)\cos\delta \\ &\quad - |P/T|^2\sin 2\phi_1]/\mathcal{R}, \\ \mathcal{A}_{\pi\pi} &= -[2|P/T|\sin(\phi_2 + \phi_1)\sin\delta]/\mathcal{R}, \\ \mathcal{R} &= 1 - 2|P/T|\cos\delta\cos(\phi_2 + \phi_1) + |P/T|^2, \end{aligned} \quad (6)$$

where $\delta \equiv \delta_P - \delta_T$. We take $-180^\circ \leq \delta \leq 180^\circ$. When $\mathcal{A}_{\pi\pi}$ is positive and $0^\circ < \phi_1 + \phi_2 < 180^\circ$, δ is negative.

Recent theoretical estimates prefer $|P/T| \sim 0.3$ with large uncertainties [26, 27, 28, 29]. Figures 9(a)-(e) show the regions for ϕ_2 and δ corresponding to the 68.3% C.L., 95.5% C.L. and 99.73% C.L. region of $\mathcal{A}_{\pi\pi}$ and $\mathcal{S}_{\pi\pi}$ (shown in Fig. 8) for representative values of $|P/T|$ and ϕ_1 . Note that a value of $(\mathcal{S}_{\pi\pi}, \mathcal{A}_{\pi\pi})$ inside the 68.3% C.L. contour requires a value of $|P/T|$ greater than ~ 0.3 .

The allowed region is not very sensitive to variations of ϕ_1 within the errors of the measurements, as can be seen by comparing Figs. 9(a), (c) and (e). The range of ϕ_2 that corresponds to the 95.5% C.L. region of $\mathcal{A}_{\pi\pi}$ and $\mathcal{S}_{\pi\pi}$ in Fig. 8 is

$$78^\circ \leq \phi_2 \leq 152^\circ,$$

for $\phi_1 = 23.5^\circ$ and $0.15 \leq |P/T| \leq 0.45$. The result is in agreement with constraints on the unitarity triangle from other measurements [31].

X. CONCLUSION

In summary, we have performed an improved measurement of CP violation parameters in $B^0 \rightarrow \pi^+\pi^-$ decays. An unbinned maximum likelihood fit to 760 $B^0 \rightarrow \pi^+\pi^-$ candidates, which contain $163^{+24}_{-23}(\text{stat})$ $\pi^+\pi^-$ signal events, yields $\mathcal{A}_{\pi\pi} = +0.77 \pm 0.27(\text{stat}) \pm 0.08(\text{syst})$, and $\mathcal{S}_{\pi\pi} = -1.23 \pm 0.41(\text{stat})^{+0.08}_{-0.07}(\text{syst})$, where the statistical uncertainties are determined from MC pseudo-experiments. This result is consistent with our previous measurement [10] and supersedes it. We obtain confidence intervals for CP -violating asymmetry parameters $\mathcal{A}_{\pi\pi}$ and $\mathcal{S}_{\pi\pi}$ based on the Feldman-Cousins approach where we use MC pseudo-experiments to determine acceptance regions. We rule out the CP -conserving case, $\mathcal{A}_{\pi\pi} = \mathcal{S}_{\pi\pi} = 0$, at the 99.93% confidence level.

The result for $\mathcal{S}_{\pi\pi}$ indicates that mixing-induced CP violation is large, and the large $\mathcal{A}_{\pi\pi}$ term is an indication of direct CP violation in B meson decay. Constraints within the Standard Model on the CKM angle ϕ_2 and the hadronic phase difference between the tree (T) and penguin (P) amplitudes are obtained for $|P/T|$ values that are favored theoretically. We find an allowed region of ϕ_2 that is consistent with constraints on the unitarity triangle from other measurements.

ACKNOWLEDGMENTS

We wish to thank the KEKB accelerator group for the excellent operation of the KEKB accelerator. We acknowledge support from the Ministry of Education, Culture, Sports, Science, and Technology of Japan and the Japan Society for the Promotion of Science; the Australian Research Council and the Australian Department of Industry, Science and Resources; the National Science Foundation of China under contract No. 10175071; the Department of Science and Technology of India; the BK21 program of the Ministry of Education of Korea and the CHEP SRC program of the Korea Science and Engineering Foundation; the Polish State Committee for Scientific Research under contract No. 2P03B 17017; the Ministry of Science and Technology of the Russian Federation; the Ministry of Education, Science and Sport of the Republic of Slovenia; the National Science Council and the Ministry of Education of Taiwan; and the U.S. Department of Energy.

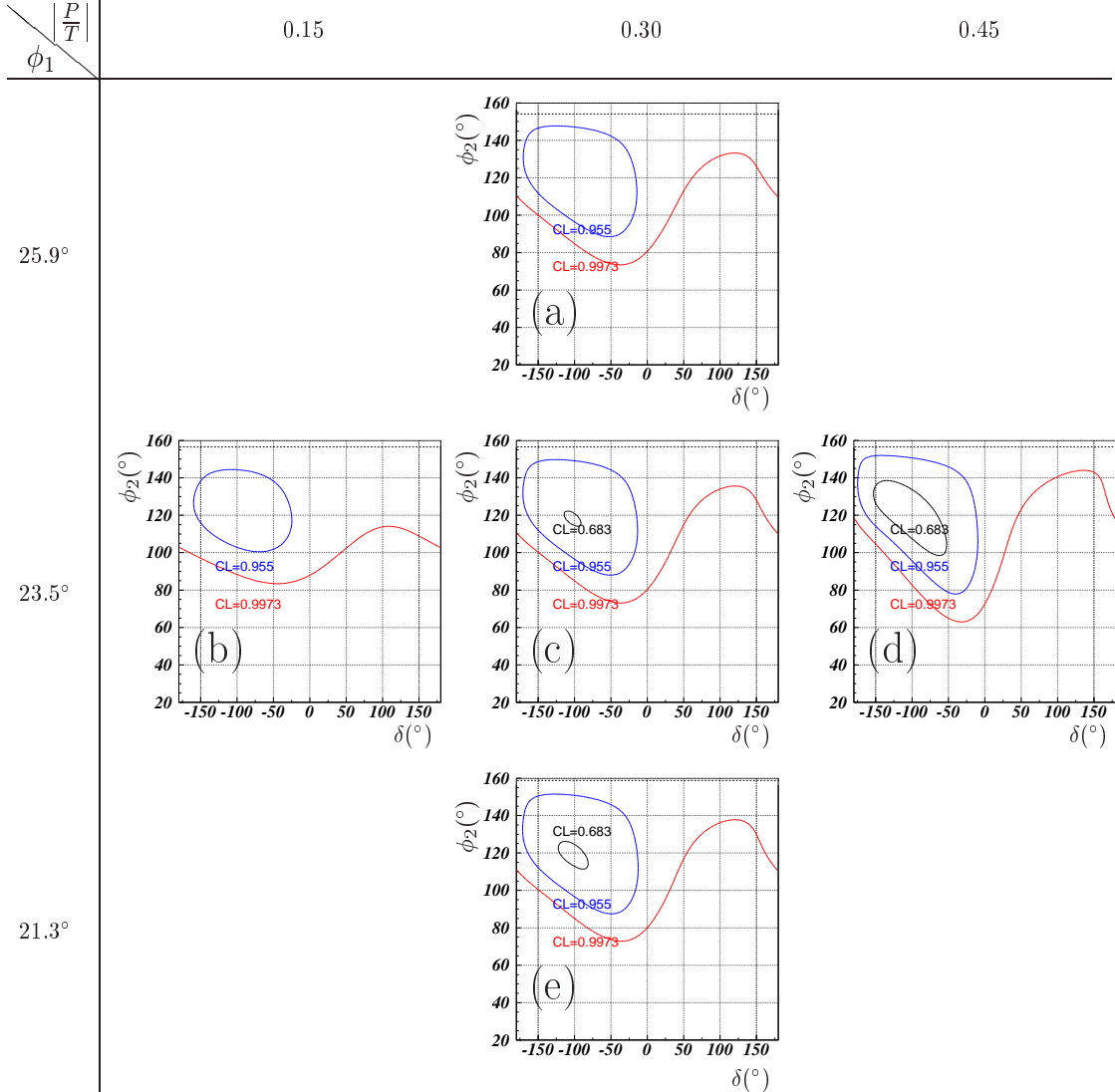


FIG. 9: The regions for ϕ_2 and δ corresponding to the 68.3%, 95.5%, and 99.73% C.L. regions of $\mathcal{A}_{\pi\pi}$ and $\mathcal{S}_{\pi\pi}$ in Fig. 8 for (a) $\phi_1 = 25.9^\circ$, $|P/T|=0.3$, (b) $\phi_1 = 23.5^\circ$, $|P/T|=0.15$, (c) $\phi_1 = 23.5^\circ$, $|P/T|=0.3$, (d) $\phi_1 = 23.5^\circ$, $|P/T|=0.45$, and (e) $\phi_1 = 21.3^\circ$, $|P/T|=0.3$. The horizontal dashed lines correspond to $\phi_2 = 180^\circ - \phi_1$.

APPENDIX A: MC PSEUDO-EXPERIMENTS AND CONFIDENCE REGIONS

We use ensembles of Monte Carlo (MC) pseudo-experiments to determine the significance of our measurement and obtain confidence regions. They are also used for various crosschecks. Each pseudo-experiment consists of events that are generated with the nominal PDFs, which are incorporated in Eq. 3. Since the parameters in the PDFs are derived from large-statistics control samples and sideband events, the pseudo-experiments precisely reproduce Δt distributions that are consistent with data. In particular, they are free from possible discrepancies between data and GEANT-based detector simulation.

To generate each event in a pseudo-experiment, we first choose one $LR-r$ region m randomly from a population that is based on the regional event fractions obtained from data.

We then generate ΔE and M_{bc} values with distributions that are determined by the event fractions $g_{\pi\pi}^m$, $g_{K\pi}^m$ and $g_{q\bar{q}}^m$, which are listed in Table II. The values of the probability functions $f_{\pi\pi}^m$, $f_{K\pi}^m$ and $f_{q\bar{q}}^m$ (in Eq. 3) are determined from the ΔE and M_{bc} values. We randomly choose an event type, $\pi\pi$, $K\pi$, $q\bar{q}$ or outlier, from a population based on $f_{\pi\pi}^m$, $f_{K\pi}^m$, $f_{q\bar{q}}^m$, and the outlier fraction f_{ol} . We generate q , Δt and resolution parameters according to the PDF of the selected event type.

We repeat this procedure until the number of events reaches the observed number of events (760 events), and perform an unbinned maximum likelihood fit to obtain $x_{\mathcal{A}_{\pi\pi}}$ and $x_{\mathcal{S}_{\pi\pi}}$, which are the fit results and should be distinguished from the true (input) values $\mathcal{A}_{\pi\pi}$ and $\mathcal{S}_{\pi\pi}$. To account for the systematic error, each fit result is further modified by an amount determined from a Gaussian variation. We test the entire procedure using GEANT simulation, and find that distributions of $x_{\mathcal{A}_{\pi\pi}}$ and $x_{\mathcal{S}_{\pi\pi}}$ obtained from the GEANT experiments are in good agreement with those from pseudo-experiments, when the resolution functions in the PDF are extracted from a lifetime fit to the GEANT data. We also verify that there is no fit bias as shown in Fig. 10.

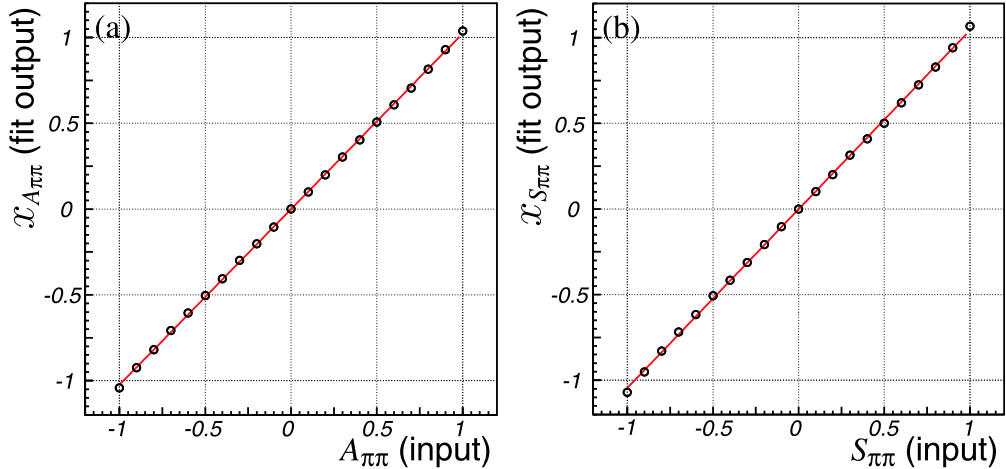


FIG. 10: Mean values of fit results vs. input values of MC pseudo-experiments for (a) $\mathcal{A}_{\pi\pi}$ and (b) $\mathcal{S}_{\pi\pi}$. The solid lines are linear fit results.

We adopt the Feldman-Cousins frequentist approach [22], which is based on the likelihood-ratio ordering principle, to obtain the confidence regions that are shown in Fig. 8 [32]. In the following, we first illustrate how we can obtain 1-dimensional confidence intervals for $\mathcal{A}_{\pi\pi}$ with $\mathcal{S}_{\pi\pi}$ set to zero; intervals for $\mathcal{S}_{\pi\pi}$ are obtained in a very similar way. We then explain the method used for the determination of the two-dimensional confidence regions for $\mathcal{A}_{\pi\pi}$ and $\mathcal{S}_{\pi\pi}$, which is an extension of that for the 1-dimensional case.

We generate 10,000 experiments for 317 sets of $(\mathcal{A}_{\pi\pi}, \mathcal{S}_{\pi\pi})$ values that cover the entire physical region. The fit to each set of experiments yields an $x_{\mathcal{A}_{\pi\pi}}$ distribution that depends on the input $\mathcal{A}_{\pi\pi}$ value. To account for this dependence, we use a PDF for $x_{\mathcal{A}_{\pi\pi}}$ that consists of two Gaussian functions whose parameters depend on $\mathcal{A}_{\pi\pi}$:

$$P(x_{\mathcal{A}_{\pi\pi}} | \mathcal{A}_{\pi\pi}) = f_A \cdot G(x_{\mathcal{A}_{\pi\pi}}; m_1, \sigma_1) + (1 - f_A) \cdot G(x_{\mathcal{A}_{\pi\pi}}; m_2, \sigma_2),$$

where $G(x; m, \sigma)$ represents a Gaussian function with mean m and standard deviation σ , and f_A , $m_{1(2)}$, and $\sigma_{1(2)}$ are polynomials of $\mathcal{A}_{\pi\pi}$. The explicit expressions for f_A , m_1 , m_2 , σ_1 and σ_2 are

$$\begin{aligned} f_A &= a_1 + a_2 \mathcal{A}_{\pi\pi}^2, \\ m_1 &= a_3 + a_4 \mathcal{A}_{\pi\pi}, \\ \sigma_1 &= a_5 + a_6 \mathcal{A}_{\pi\pi}^2, \\ m_2 &= a_7 + a_8 \mathcal{A}_{\pi\pi} + a_9 \mathcal{A}_{\pi\pi}^2 + a_{10} \mathcal{A}_{\pi\pi}^3, \\ \sigma_2 &= a_{11} + a_{12} \mathcal{A}_{\pi\pi}, \end{aligned}$$

where the 12 free parameters (a_i , $i = 1, 12$) are determined from an unbinned maximum-likelihood fit to the $x_{\mathcal{A}\pi\pi}$ distributions. Figures 11(a) and (b) show the distributions and the $x_{\mathcal{A}\pi\pi}$ PDF for the cases $(\mathcal{A}_{\pi\pi}, \mathcal{S}_{\pi\pi}) = (0, 0)$ and $(\mathcal{A}_{\pi\pi}, \mathcal{S}_{\pi\pi}) = (+1, 0)$, respectively. The PDFs are in good agreement with the distributions of pseudo-experiments in both cases.

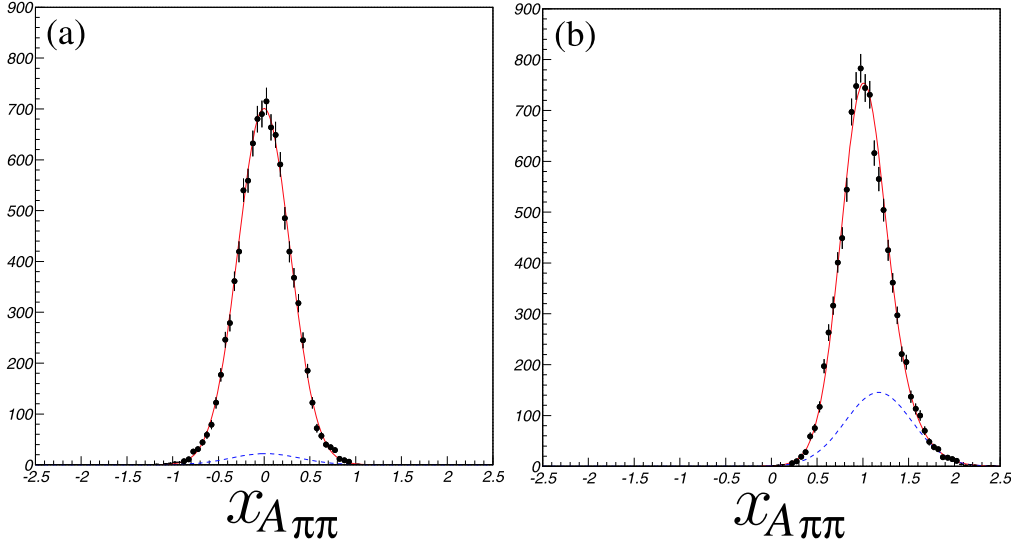


FIG. 11: $x_{\mathcal{A}\pi\pi}$ distributions and the PDFs for (a) $(\mathcal{A}_{\pi\pi}, \mathcal{S}_{\pi\pi}) = (0, 0)$ and (b) $(\mathcal{A}_{\pi\pi}, \mathcal{S}_{\pi\pi}) = (+1, 0)$. Solid and dashed curves represent the total PDFs and the second Gaussian components, respectively.

The acceptance region $[x_{\mathcal{A}1}, x_{\mathcal{A}2}]$ for a given $\mathcal{A}_{\pi\pi}$ and a confidence level α is defined by:

$$\alpha = \int_{x_{\mathcal{A}1}}^{x_{\mathcal{A}2}} dx_{\mathcal{A}\pi\pi} P(x_{\mathcal{A}\pi\pi} | \mathcal{A}_{\pi\pi}).$$

We adopt the likelihood-ratio ordering principle to determine $x_{\mathcal{A}1}$ and $x_{\mathcal{A}2}$. Using the likelihood-ratio

$$LR(x_{\mathcal{A}\pi\pi} | \mathcal{A}_{\pi\pi}) \equiv P(x_{\mathcal{A}\pi\pi} | \mathcal{A}_{\pi\pi}) / P(x_{\mathcal{A}\pi\pi} | \mathcal{A}_{\text{best}}),$$

where $\mathcal{A}_{\text{best}}$ gives the maximum P value for a given $x_{\mathcal{A}\pi\pi}$, we require

$$LR(x_{\mathcal{A}\pi\pi} | \mathcal{A}_{\pi\pi}) \geq LR(x_{\mathcal{A}1} | \mathcal{A}_{\pi\pi}) = LR(x_{\mathcal{A}2} | \mathcal{A}_{\pi\pi})$$

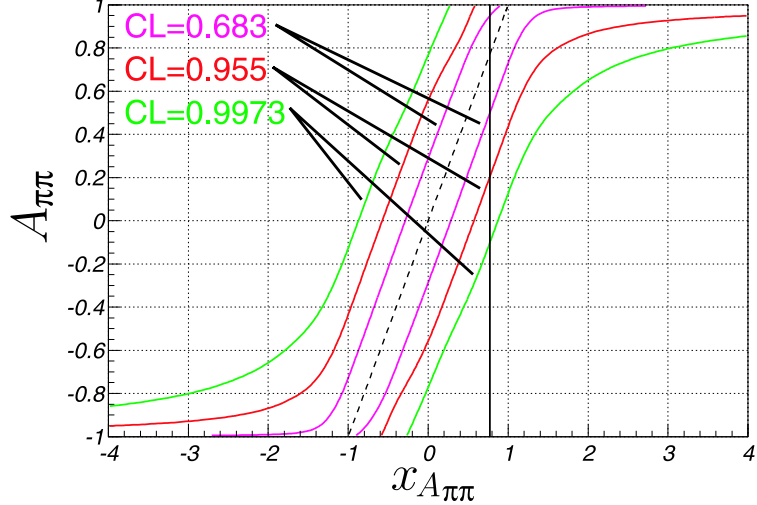


FIG. 12: Confidence belts in the $\mathcal{A}_{\pi\pi}$ versus $x_{\mathcal{A}_{\pi\pi}}$ plane for $\alpha = 0.683$, 0.955 , and 0.9973 in the one-dimensional case. The dashed line corresponds to $\mathcal{A}_{\pi\pi} = x_{\mathcal{A}_{\pi\pi}}$.

for any $x_{\mathcal{A}_{\pi\pi}}$ in $[x_{\mathcal{A}1}, x_{\mathcal{A}2}]$. Figure 12 shows the resulting confidence belts for $\mathcal{A}_{\pi\pi}$. For a given measurement $x_{\mathcal{A}_{\pi\pi}}$, a confidence interval at a confidence level α is obtained from the figure.

The procedure to obtain the 2-dimensional confidence regions for $\mathcal{A}_{\pi\pi}$ and $\mathcal{S}_{\pi\pi}$ (Fig. 8) is an extension of the method described above. We use the following PDF:

$$\begin{aligned} P(x_{\mathcal{A}_{\pi\pi}}, x_{\mathcal{S}_{\pi\pi}} | \mathcal{A}_{\pi\pi}, \mathcal{S}_{\pi\pi}) \\ = f_{AS} \cdot G(\mathcal{A}_{\pi\pi}; m_{A1}, \sigma_{A1}) \cdot G(\mathcal{S}_{\pi\pi}; m_{S1}, \sigma_{S1}) \\ + (1 - f_{AS}) \cdot G(\mathcal{A}_{\pi\pi}; m_{A2}, \sigma_{A2}) \cdot G(\mathcal{S}_{\pi\pi}; m_{S2}, \sigma_{S2}), \end{aligned}$$

where f_{AS} , $m_{A1(2)}$, $m_{S1(2)}$, $\sigma_{A1(2)}$ and $\sigma_{S1(2)}$ depend both on $\mathcal{A}_{\pi\pi}$ and $\mathcal{S}_{\pi\pi}$. There are 27 free parameters that are determined from an unbinned maximum-likelihood fit to the $(x_{\mathcal{A}_{\pi\pi}}, x_{\mathcal{S}_{\pi\pi}})$ distributions. We find that the PDFs represent the distributions of $x_{\mathcal{A}_{\pi\pi}}$ and $x_{\mathcal{S}_{\pi\pi}}$ very well for the input $\mathcal{A}_{\pi\pi}$ and $\mathcal{S}_{\pi\pi}$ values over the entire physical region. An acceptance region Ω at a confidence level α is also defined in a similar way to that for the 1-dimensional case:

$$\alpha = \int_{\Omega} dx_{\mathcal{A}_{\pi\pi}} dx_{\mathcal{S}_{\pi\pi}} P(x_{\mathcal{A}_{\pi\pi}}, x_{\mathcal{S}_{\pi\pi}} | \mathcal{A}_{\pi\pi}, \mathcal{S}_{\pi\pi}),$$

where likelihood-ratio ordering is used. Using the requirement

$$LR(x_{\mathcal{A}_{\pi\pi}}, x_{\mathcal{S}_{\pi\pi}} | \mathcal{A}_{\pi\pi}, \mathcal{S}_{\pi\pi}) \geq LR(+0.77, -1.23 | \mathcal{A}_{\pi\pi}, \mathcal{S}_{\pi\pi})$$

which corresponds to an acceptance region with our measurement $(x_{\mathcal{A}_{\pi\pi}}, x_{\mathcal{S}_{\pi\pi}}) = (+0.77, -1.23)$ at its boundary, we scan the physical region in the $\mathcal{A}_{\pi\pi}$ - $\mathcal{S}_{\pi\pi}$ plane and calculate a confidence level α for each input point $(\mathcal{A}_{\pi\pi}, \mathcal{S}_{\pi\pi})$ to obtain the confidence regions shown in Fig. 8.

APPENDIX B: SOURCE OF SMALL MINOS ERRORS

The Feldman-Cousins approach with acceptance regions determined from MC pseudo-experiments, which is described in Appendix A, is applicable to a wide range of analyses. On the other hand, care is needed when using experimental MINOS errors for the confidence interval calculation, as mentioned in Sec. VIII A. In particular, difficulties may arise when the number of events is not large and the true values of physical parameters are located close to a physical boundary. In such a case, a small number of events can have a large influence on both the size of the MINOS errors and the shape of the log-likelihood ratio curve. The likelihood function for some events may become negative when the fit parameters are beyond the physical boundary.

The observed features of the MINOS errors arise when there is an event that restricts the fit parameters in or close to the physical region, while the fit to all the other events gives a maximum likelihood that is located outside the physical region and is not allowed by the aforementioned restrictive event. For example, in this fit the removal of such a restrictive event results in an $\mathcal{S}_{\pi\pi}$ value that is more negative than $\mathcal{S}_{\pi\pi} = -1.23$ (further from the physical boundary). In this case, the log-likelihood ratio curve is deformed by inclusion of the restrictive event, even if the curve before the inclusion is well-described by a parabola. The sizes of the MINOS errors also become small.

We investigate this type of single-event fluctuation and its relation to the size of the MINOS errors with MC pseudo-experiments. For each experiment, we repeat the fit by removing each event in turn. The event that creates the largest difference in $\mathcal{S}_{\pi\pi}$ is tagged as the restrictive event and the change produced by the removal of the restrictive event, $\Delta\mathcal{S}_{\pi\pi}$, is recorded. When we choose the point of maximum likelihood at the physical boundary ($\mathcal{A}_{\pi\pi}, \mathcal{S}_{\pi\pi} = (+0.57, -0.82)$) as the input for the MC pseudo-experiments, we obtain the average values of $\Delta\mathcal{S}_{\pi\pi}$ as a function of the positive error of $\mathcal{S}_{\pi\pi}$ shown in Fig. 13. The correlation between the size of the error and the single-event fluctuation is evident.

In our data, we have one event that has a large effect on the sizes of MINOS errors. The removal of this event from the fit gives $\mathcal{S}_{\pi\pi} = -1.91^{+0.36}_{-0.33}$ and $\mathcal{A}_{\pi\pi} = 0.64^{+0.19}_{-0.20}$, where the errors are MINOS errors; $\mathcal{S}_{\pi\pi}$ is shifted to a more negative value ($\Delta\mathcal{S}_{\pi\pi} = -0.67$) and the MINOS error increases. This event has $qr = -0.92$ which is close to unambiguous B flavor assignment and corresponds to a very small wrong-tag probability. In addition, this event has $\Delta E = -0.01$ GeV, and $LR = 0.98$, which corresponds to small $B^0 \rightarrow K^+\pi^-$ and $q\bar{q}$ background probabilities. For this event, $\Delta t = -3.8$ ps and, thus, $\sin(\Delta m_d \Delta t) \approx -1$. According to Eq. 3, this event has a negative likelihood value at negative $\mathcal{S}_{\pi\pi}$ values beyond ~ -1.5 , where it truncates the log-likelihood ratio curve. As a result, the negative MINOS error for the entire event sample is restricted by this single event.

As shown in Fig. 13, the observed single-event fluctuation $\Delta\mathcal{S}_{\pi\pi} = -0.67$ is consistent with the expectation from the MC pseudo-experiments if the positive error of $\mathcal{S}_{\pi\pi}$ is $\sim +0.24$, which is the case for our data. A similar study for input values of $\mathcal{S}_{\pi\pi}$ and $\mathcal{A}_{\pi\pi}$ that are well within the physically allowed region indicates that this behavior occurs much less often.

[1] M. Kobayashi and T. Maskawa, Prog. Theor. Phys. **49**, 652 (1973).
[2] Belle Collaboration, K. Abe *et al.*, Phys. Rev. Lett. **87**, 091802 (2001); Belle Collaboration, K. Abe *et al.*, Phys. Rev. D **66**, 032007 (2002).

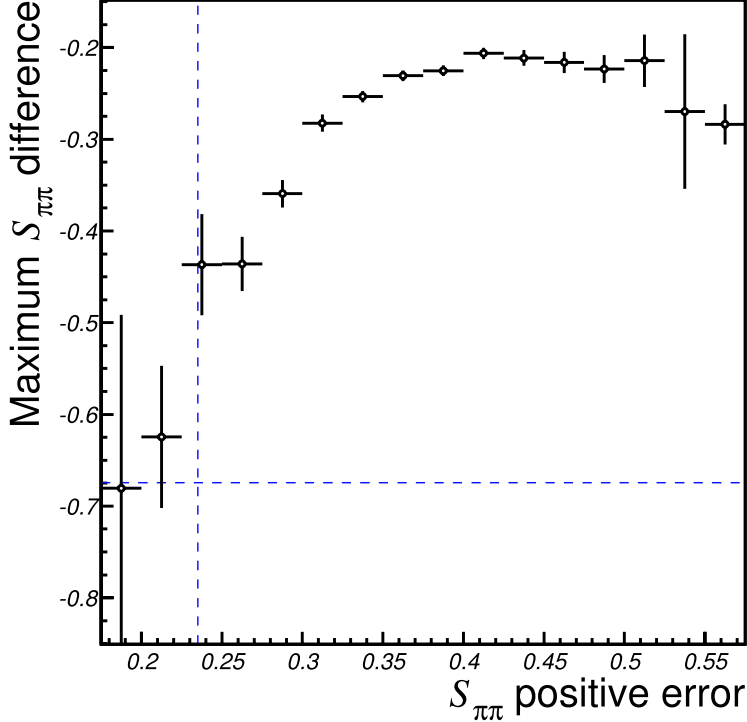


FIG. 13: Single-event fluctuation versus the positive MINOS error on $S_{\pi\pi}$. The dashed lines indicate the observed $\Delta S_{\pi\pi}$ and $S_{\pi\pi}$ positive MINOS error.

- [3] Belle Collaboration, K. Abe *et al.*, Phys. Rev. D **66**, 071102 (2002).
- [4] BaBar Collaboration, B. Aubert *et al.*, Phys. Rev. Lett. **87**, 091801 (2001); BaBar Collaboration, B. Aubert *et al.*, Phys. Rev. D **66**, 032003 (2002); BaBar Collaboration, B. Aubert *et al.*, Phys. Rev. Lett. **89**, 201802 (2002).
- [5] A. B. Carter and A. I. Sanda, Phys. Rev. D **23**, 1567 (1981); I. I. Bigi and A. I. Sanda, Nucl. Phys. **B193**, 85 (1981).
- [6] A general review of the formalism is given in I.I. Bigi, V.A. Khoze, N.G. Uraltsev, and A.I. Sanda, “*CP* Violation” page 175, ed. C. Jarlskog, World Scientific, Singapore (1989).
- [7] Throughout this paper, the inclusion of the charge conjugate mode decay is implied unless otherwise stated.
- [8] ϕ_1 ($= \beta$) $\equiv \arg[-V_{cd}V_{cb}^*/V_{td}V_{tb}^*]$ and ϕ_2 ($= \alpha$) $\equiv \arg[-V_{td}V_{tb}^*/V_{ud}V_{ub}^*]$.
- [9] M. Gronau, Phys. Rev. Lett. **63**, 1451 (1989); D. London and R. Peccei, Phys. Lett. B **223**, 257 (1989); M. Beneke, G. Buchalla, M. Neubert and C. T. Sachrajda, Nucl. Phys. B **606**, 245 (2001); Y. Y. Keum, H-N. Li and A. I. Sanda, Phys. Rev. D **63**, 054008 (2001); M. Ciuchini *et al.*, Phys. Lett. B **515**, 33 (2001); M. Gronau and J. L. Rosner, Phys. Rev. D **65**, 013004 (2002).
- [10] Belle Collaboration, K. Abe *et al.*, Phys. Rev. Lett. **89**, 071801 (2002). $S_{\pi\pi} = -1.21^{+0.38}_{-0.27}(\text{stat})^{+0.16}_{-0.13}(\text{syst})$ and $\mathcal{A}_{\pi\pi} = +0.94^{+0.25}_{-0.31}(\text{stat}) \pm 0.09(\text{syst})$. In this paper, the statistical uncertainties were determined from the observed fitting errors rather than from MC pseudo-experiments as in the analysis described here. Thus, the errors here are larger than those obtained by scaling the previous errors by the integrated luminosities.
- [11] $S_{\pi\pi} = 0.02 \pm 0.34(\text{stat}) \pm 0.05(\text{syst})$ and $C_{\pi\pi} = -0.30 \pm 0.25(\text{stat}) \pm 0.04(\text{syst})$ in BaBar

Collaboration, B. Aubert *et al.*, hep-ex/0207055, to be published in Phys. Rev. Lett. Note that the sign convention for the coefficient of the cosine term $C_{\pi\pi}$ defined in the above reference is opposite to our convention, i.e. $C_{\pi\pi} = -\mathcal{A}_{\pi\pi}$.

- [12] E. Kikutani ed., KEK Preprint 2001-157 (2001), to appear in Nucl. Instr. and Meth. A.
- [13] Belle Collaboration, A. Abashian *et al.*, Nucl. Instr. and Meth. A **479**, 117 (2002).
- [14] Belle Collaboration, B.C.K Casey *et al.*, Phys. Rev. D **66**, 092002 (2002).
- [15] The Fox-Wolfram moments were introduced in G. C. Fox and S. Wolfram, Phys. Rev. Lett. **41**, 1581 (1978). The Fisher discriminant used by Belle is described in [14] and Belle Collaboration, K. Abe *et al.*, Phys. Lett. B **511**, 151 (2001).
- [16] CERN Program Library Long Writeup W5013, CERN, 1993.
- [17] ARGUS Collaboration, H. Albrecht *et al.*, Phys. Lett. B **241**, 278 (1990).
- [18] We use Eq. (28.9) in Particle Data Group, D. E. Groom *et al.*, Eur. Phys. J. C **15**, 1 (2000) p.196.
- [19] We obtain MINOS errors $^{+0.20}_{-0.23}$ for $\mathcal{A}_{\pi\pi}$ and $^{+0.24}_{-0.15}$ for $\mathcal{S}_{\pi\pi}$ for data, while the MC pseudo-experiments yield $^{+0.24}_{-0.26}$ for $\mathcal{A}_{\pi\pi}$ and $^{+0.36}_{-0.32}$ for $\mathcal{S}_{\pi\pi}$ with the input values at the boundary and ± 0.27 for $\mathcal{A}_{\pi\pi}$ and ± 0.37 for $\mathcal{S}_{\pi\pi}$ at $\mathcal{A}_{\pi\pi} = \mathcal{S}_{\pi\pi} = 0$. The correlation between $\mathcal{A}_{\pi\pi}$ and $\mathcal{S}_{\pi\pi}$ is found to be 0.024 for data.
- [20] Belle Collaboration, K. Suzuki, to appear in the proceedings of XXXI International Conference on High Energy Physics, Amsterdam, the Netherlands, July 24-31, 2002.
- [21] Particle Data Group, K. Hagiwara *et al.*, Phys. Rev. D **66**, 010001-1 (2002).
- [22] G. J. Feldman and R. D. Cousins, Phys. Rev. D **57**, 3873 (1998).
- [23] I.I. Bigi, Phys. Lett. B **535**, 155 (2002).
- [24] L. Wolfenstein and F. Wu, Europhys. Lett. 58, 49 (2002).
- [25] M. Gronau and J.L. Rosner, Phys. Rev. D **65**, 093012 (2002).
- [26] M. Gronau and J.L. Rosner, Phys. Rev. D **65**, 013004 (2002).
- [27] Z. Luo and J.L. Rosner, Phys. Rev. D **65**, 054027 (2002).
- [28] M. Beneke, G. Buchalla, M. Neubert, and C. T. Sachrajda, Nucl. Phys. B **606**, 245 (2001).
- [29] The authors of Ref. [26] use $SU(3)$ flavor symmetry to estimate $|P|$ from the measured $B \rightarrow K^0\pi^+$ decay rate, and factorization [27] to estimate $|T|$ from the decay rate for $B \rightarrow \pi\ell\nu$.
- [30] Using the average of recent values of $\sin 2\phi_1$ from Belle [3] and BaBar [4], we obtain $\phi_1 = (23.5^{+2.4}_{-2.2})^\circ$.
- [31] Y. Nir, hep-ph/0208080, to appear in the proceedings of XXXI International Conference on High Energy Physics, Amsterdam, Netherlands, July 24-31, 2002.
- [32] T. Nakadaira, PhD thesis, The University of Tokyo (2003).